

## X-ray Diffraction of Bent Crystals in Bragg Geometry. I. Perfect-Crystal Modelling

BY C. T. CHANTLER\*

*Clarendon Laboratory, University of Oxford, Parks Road, Oxford OX1 3PU, England*

(Received 23 April 1991; accepted 5 May 1992)

### Abstract

X-ray reflectivity, widths, centroid shifts and profiles for curved perfect crystals are calculated from a model. The crystal is approximated by a stack of perfect-crystal lamellae or blocks with a gradually changing (mean) orientation. A computer program has been developed to calculate the above quantities in the Johann geometry for the composite crystal from the dynamic theory of diffraction. Focusing and defocusing aberrations and the use of photographic detection methods are included. Correction of omissions from earlier theory and modelling is noted, together with observed effects. Incoherent scattering can give dramatic changes in diffracted intensities and significant shifts of final parameters. Effects of depth penetration on shifts, cosine ratios and other parameters are included. Assumptions of the model and implementation are detailed. It is shown that interference effects between waves of roughly equal amplitudes require use of lamellar thicknesses greater than those corresponding to the Darwin range. Internal tests demonstrate agreement with the literature at extremes. The theory is applied to first- and fourth-order spectra in differential Lyman  $\alpha$  wavelength measurements. Results for pentaerythritol 002 crystals are presented. Paper II of this series extends this model to non-ideally imperfect crystals and other crystals of interest and discusses experimental agreement.

### 1. Introduction

Extraction of the Lamb shifts and Lyman  $\alpha$  wavelengths for medium-Z systems in fourth-order transitions by comparison with first-order transitions involves accounting for several systematic shifts, the largest of which are diffraction shifts. These are of the order of 1 part in  $10^4$  of the wavelengths or 13–17% of the Lamb shift, so any attempt to obtain accuracy below this level must account for them. Lines of the same diffraction order, with energies within a factor of two of one another, show large variation of these shifts with respect to the diffracting angle.

Diffraction of X-rays in Bragg and Laue geometries by flat perfect crystals is well understood (Zachariassen, 1945; James, 1963; Hirsch & Ramachandran, 1950; Cole & Stemple, 1962; Batterman & Cole, 1964) and has been studied and tested in crystals where these assumptions hold to a good first approximation (Källne & Aberg, 1975; Bearden, Marzolf & Thomsen, 1968; Deslattes, Torgeson, Paretzkin & Horton, 1966).

Theories for diffraction by perfect curved (*i.e.* stressed) crystals have been developed (White, 1950; Taupin, 1964; Takagi, 1969). Models following an eikonal approximation based on rays were developed and solved for the Laue geometry, and solutions of wave equations were presented for the Laue case with a spherical incident wave (Katagawa & Kato, 1974; Chukhovskii & Petrashen', 1977). Forms of solution in Bragg reflection for thick crystals in certain limits have been developed (Chukhovskii, Gabrielyan & Petrashen', 1978; Chukhovskii, Gabrielyan, Kislovskii & Prokopenko, 1987; Chukhovskii & Malgrange, 1989) but precision calculation of profiles or extension to non-ideal crystals has not been achieved. Standard implementations for curved-crystal Johann spectroscopy of synchrotron, stationary and fast-beam sources use idealized crystal elements, neglecting centroid, width and profile effects (Beyer & Liesen, 1988; Suortti & Freund, 1989).

Application to Lamb-shift measurements has suffered from flaws in the theory and implementation, the recognition of which has led to this investigation. This paper attempts to improve upon the earlier method for estimating diffraction parameters, to develop a theory to account for major effects in curved crystals, and to include other significant contributions to the first–fourth order and other relative shifts. It presents a general model for finite curved perfect crystals. This highlights assumptions retained with a view to deriving reliable refractive-index order shifts, profiles and diffracted intensities from a curved diffracting crystal in the Bragg geometry. The current purpose is to understand profiles and shifts in the Johann mounting on photographic film, including shifts and focusing from Rowland-circle aberrations and asymmetric depth penetration of the emulsion. These are evaluated, since emphasis is on production

\*Present address: Quantum Metrology Division, National Institute of Standards and Technology, Gaithersburg, MD 20899, USA.

of corrections to centroid positions in experimental data rather than being primarily concerned with reflectivities. Paper II extends this model to non-ideally imperfect crystals and all simpler subclasses and presents comparison with experiment.

## 2. Earlier models for finite curved perfect crystals

Diffraction theories of electrons and X-rays by perfect curved crystals are commonly based on the division of the crystal into lamellae parallel to the surface, with relations between boundary conditions at each lamellar surface governed by wave-optical principles. A development of the theory, applied to X-ray diffraction from neutron diffraction studies, followed Zachariassen (1945) and formulae for perfect finite crystals (Boeuf *et al.*, 1978) applied to the Bragg geometry. This was continued by Caciuffo, Melone, Rustichelli & Boeuf (1987), hereinafter referred to as CMRB. This paper forms the basis of the present discussion. Suortti, Pattison & Weyrich (1986), Popovici, Stoica, Chalupa & Mikula (1988) and Erola, Etläniemi, Suortti, Pattison & Thomlinson (1990) have used similar models.

Fig. 1 illustrates the main assumptions of this perfect curved crystal model. Assumptions (I) to (VII) are detailed in CMRB but may be summarized as treating the curved crystal as a series of flat rectangular thin crystals of thickness  $\Delta y = 2$  where  $y$  is a diffraction coordinate defined in the Appendix together with other notation. The orientation of each layer is that of the central plane of the layer. Adjacent regions will generally *not* multiply scatter primary and diffracted beams because of the crystal curvature. Interference and coherent scattering is dominated by a localized region within the crystal for any given incident angle. Main profile contributions arise from layers where  $y \simeq 0$ , known as region 2, and reflectivities at the surface are calculated from the energy balance. For a given layer  $j$ , an incident power  $T_{j-1} = \prod_{i=0}^{j-1} t_i P_0^0$  yields diffracted and transmitted powers  $R_{j-1} = T_{j-1} r_j$  and  $T_j = T_{j-1} t_j$  where  $r_j$  is the reflectivity and  $t_j$  is the transmitted relative intensity for the  $j$ th layer. Then,

$$R = \sum_{j=1}^n R_j \exp(-\mu S_j), \quad (1)$$

where  $S_j$  is the X-ray path length from the front of the  $j$ th layer to the surface of the crystal. This is assumed to equal the sum of path lengths through each crystal from layer  $j-1$  to 1:

$$S_j = \sum_{k=j-1}^1 t_0 / \sin \theta_{rk}. \quad (2)$$

*Assumption VI.* For a given surface (or *first-layer*) orientation  $y(0)$ , the orientation of the  $j$ th layer  $y_j$  is

given by

$$y_j = y(0) + c A_j \quad (3)$$

with  $A_j$  related to the crystal depth and  $c$  proportional to the inverse of the radius of curvature of the crystal [equation (8.29) of CMRB; the polarization factor is omitted].

*Assumption VII.* For a given orientation  $y_j$  and thickness  $A_j$  of the  $j$ th layer, the reflectivity and ratio of transmitted to incident powers for the layer  $j$  is given by either the 'thick' or infinite flat crystal formulae [equation (7.28) *et seq.* of CMRB; see also Cole & Stemple (1962)] or more general finite crystal formulae [equations (8.48)–(8.52), CMRB]. These equations estimate the X-ray diffraction pattern  $R = R\{y(0)\}$  for the curved crystal.

The profile is near perfect for radii greater than 5 m, giving integrated reflectivities of  $R_H^y = \pi$  (negligible absorption limit). As the crystal is bent, the reflectivity approaches the mosaic or kinematic limit  $R_H^y = \pi A_a$ , where

$$T_a = (1/\mu) / [1/(\sin \theta_{inc}) + 1/(\sin \theta_{out})],$$

$$A_a^{low\ absn} = \pi |C\psi'_H| T_a / (\lambda |\gamma_0 \gamma_H|^{1/2}). \quad (4)$$

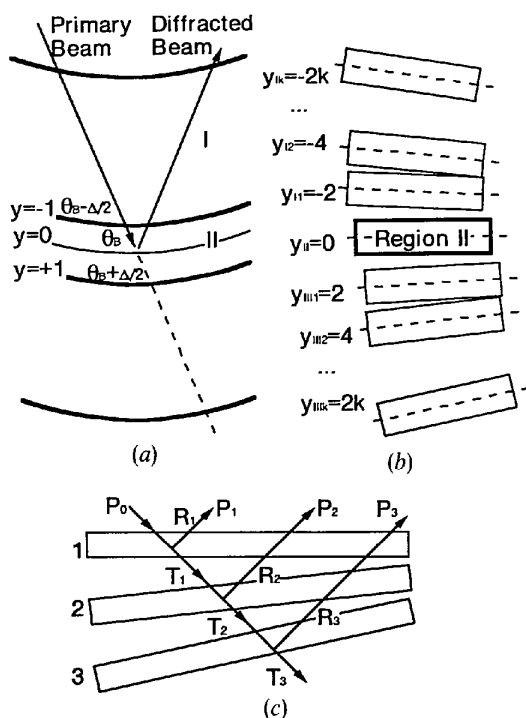


Fig. 1. Model for finite curved perfect crystals as described by Caciuffo *et al.* (1987). (a) Sketch of a narrow low-divergence monochromatic beam interacting with a real crystal, illustrating the region of the crystal diffracting in the Darwin (zero-absorption) limit. (b) Separation of the crystal into layers of perfect crystals, only one of which (region II) is assumed to interact strongly with the radiation. (c) The energy balance considered to evaluate the curved-crystal reflectivity.

Gain in reflectivity with curvature is estimated by  $A_s$ . Qualitatively, this remains valid when more appropriate formulae are used [cf. (1) and equation (6.134) of Chantler (1990); see also Cole & Stemple (1962)] or when curved-model predictions are compared with these extremes. CMRB and Boeuf *et al.* (1978) agree at the 30% level with experimental integrated reflectivities from Ge (111) and  $\alpha$ -SiO<sub>2</sub> (101) for bending radii from 0.5 to 5 m. The results test theoretical predictions but not those aspects of greatest concern herein.

### 3. Allowance for depth penetration and Johann geometry

The model above estimates profiles for a uniform source but does not consider source size and profile, finite crystal size or location of diffracting beams. Shifts of the mean  $y$  coordinate with respect to zero provide information on the mean diffracting angle with respect to the Bragg angle. They do not, however, include the geometrical shift of the beam location on the crystal surface with respect to the incident location (an effect of the depth penetration of the crystal), which shifts and broadens the partially focused image on the Rowland circle. The crystal curvature and finite source restrict the range of possible incident locations that diffract, by the variation of incident angle with surface location, which leads to this shift.

A general discussion of formulae for the Johann mounting geometry is given elsewhere (§§5.2.8–9, Chantler, 1990). In the SS1 instrument used in tests and experiments described here, the finite source lies well inside the Rowland circle and has significant angular divergence (Fig. 2). The divergence may be added to the final profile as a Gaussian convolution *via* the Doppler width. This broadens the profiles symmetrically and does not contribute a shift (the Doppler shift already being included). The source is defined by circular upstream collimators and the focus and distribution of the beam incident upon the foil. From observation of the blackening and deformation of the foil with exposure, the source may be represented by a truncated Gaussian

$$I_{\text{REL}} \propto \exp[-4(x/s_w)^2 \ln 2], \quad (5)$$

where  $s_w$  is the full width at half-maximum (FWHM) of the source and the distribution is truncated at  $|x| = 0.75s_w$ . Radiation is assumed isotropic for regions incident on the crystal and focused onto the detector, corresponding to near-normal angles of emission and a moderate range of incident angles on the crystal.

Ray tracing over angles  $\theta_s$  and position  $x$  is used, with ranges and precision giving less than 1% effects on peak and integrated reflectivities and widths, and small saw-tooth oscillations superimposed on output

profiles. The incident grazing angle  $\theta_{\text{inc}}$  and location on the crystal along the generatrix ( $XXz$ ) are defined for each ray. This yields  $\theta_A$ , subtended by  $XXz$  at the centre of the circle defined by the crystal curvature. Certain terms of relative order less than  $10^{-3}$  are neglected in this ray-tracing exercise (Chantler, 1990). Two parameters define the source centre relative to the crystal pole. Also used are the cylindrical crystal radius  $2Rz$  and the transverse angle  $\alpha_1$  of the incident beam with respect to the generatrix.

Previous treatments refer to the asymmetry parameter  $b$  as the measure of non-parallelism of the diffracting planes and the surface (CMRB; Zachariassen, 1945). This parameter is not a constant but is a function of the incident angle. Diffracting planes may

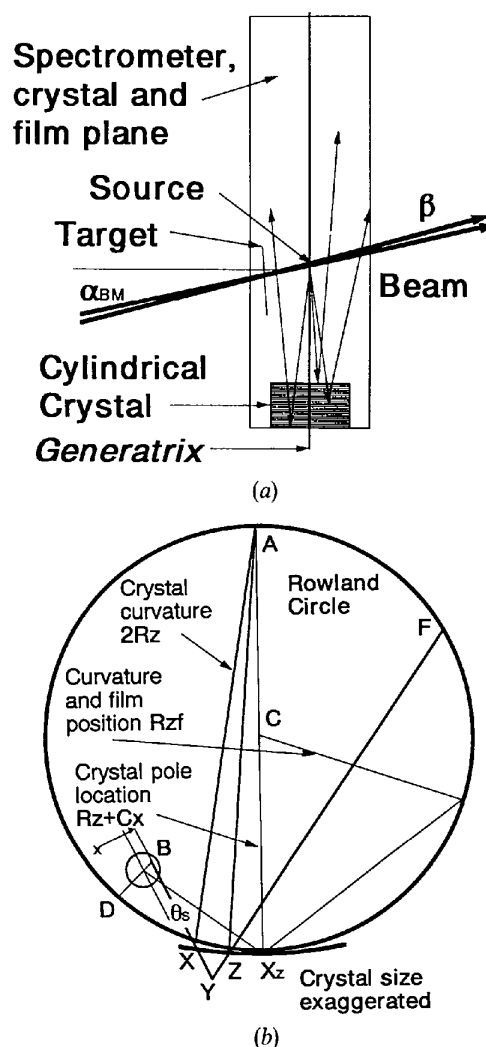


Fig. 2. Diagram of geometry of SS1 instrument. (a) View normal to generatrix; (b) Geometry on the generatrix of the diffracting crystal; additional parameters discussed in the text are  $x$ ,  $\theta_s$ ,  $\theta_1 = \pi/2 - \angle AXB$ ,  $\theta_2 = \pi/2 - \angle AZF$ ,  $\theta_A = \angle XzAX$ ,  $\theta_{Az} = \angle XzAZ$ ,  $x_{\text{line}} = ZF$ ,  $Y_{iz}$  = arc length  $XzF$ .

be expected to have a mean angle  $\alpha_{\text{plane}}$  with respect to the surface for flat or curved crystals. Use of a constant  $\alpha_{\text{plane}}$  assumes either that materials are isotropic or that  $\alpha_{\text{plane}}$  is small, but is generally the first-order contribution (*cf.* Kalman & Weissman, 1983). Then,

$$b \simeq -\sin \theta_{ik} / \sin \theta_{rk} \\ = -1 / (\cos 2\alpha_{\text{plane}} + \sin 2\alpha_{\text{plane}} \cot \theta_{ik}). \quad (6)$$

This assumes that  $\theta = \theta_r$  with respect to diffracting planes, accurate at the  $10^{-4}$  level or the level of refractive-index corrections. The component of  $\alpha_{\text{plane}}$  normal to the generatrix is observed to be negligible in our case.

$y(0)$  then follows from its definition in the Appendix and the definition of  $\alpha$ , with  $\theta_{i1} = \theta_{\text{inc}}$ . Here,  $\alpha_{\text{plane}}$  is explicitly included, compared with other papers where it is implied or neglected. This provides input variables for the model.

Each ray may be traced from this surface location and angle to the mean penetration depth and back to the surface, yielding an output grazing angle  $\theta_{\text{out}}$  and location relative to the crystal pole that may be traced to the detector location. Convolution with a final detector profile then gives the explicit shift (in units of length) of the profile around the Rowland circle (or along the detector)  $Y_{iz}$ . The shift is calculated relative to a ray tracing from the crystal surface to the detector, so that focusing and defocusing elements of the Johann mounting relating to the crystal surface lying off the Rowland circle are implicitly included. Derived shifts are primarily refractive-index corrections and diffraction shifts due to depth penetration, with small detector-profile contributions.

#### 4. Choice of diffraction coordinate

It is not specified in the model whether the diffraction depth coordinate  $y$  for the first encountered layer of the crystal should be  $y(0)$ ,  $y(0) - 1$  or a multiple of two, although the implication is that a multiple of two should be used. This suffers from the obvious flaw that the first layer will then *not* have a thickness of  $\Delta y_0 = 2$  but instead will have

$$\Delta y = -2 \text{Int} \{ -[y(0) - 1]/2 \} - y(0) + 1, \quad (7)$$

where 'Int' denotes the integer part. If it is assumed that the crystal projects from the mean surface by a thickness corresponding to  $\Delta y_0 - \Delta y$ , a single layer thickness results. A single value of reflectivity and transmission for a given layer (or crystallite) at a given incident angle may then be calculated *a priori*. Typically, this implies that crystallites project up to 0.05 mm from the surface with periodicity  $dy = \Delta y_0$ ! Alternative set-ups are illustrated in Fig. 3.

One alternative would leave all thicknesses constant so that a single finite flat crystal profile may be calculated *a priori*, defining succeeding values of  $y$  as  $y(0) + 1$ ,  $y(0) + 3, \dots$ , so that the midplane for the main diffracting region would not have  $y = 0$  but some other value. This divides the region of Darwinian total reflection between two crystallites and the large and necessary interference between these two layers would be neglected. These two 'solutions' yield no error for those cases where  $y(0)$  is *odd*, but would add an error with a period of  $dy = 2$ . This periodicity (as opposed to *Pendellösung* oscillation) may be observed in CMRB and Boeuf *et al.* (1978).

A third, although poor, solution is to follow the model but treat the first layer as having the thickness given above. Interference effects for the first layer are then largely neglected. Relevant reflectivity and transmission must be calculated explicitly for the first layer for each ray, which is computationally prohibitive, or approximated from the value for a thickness corresponding to  $\Delta y_0$ . If  $r_{t_0}$  and  $t_{t_0}$  are the reflectivity

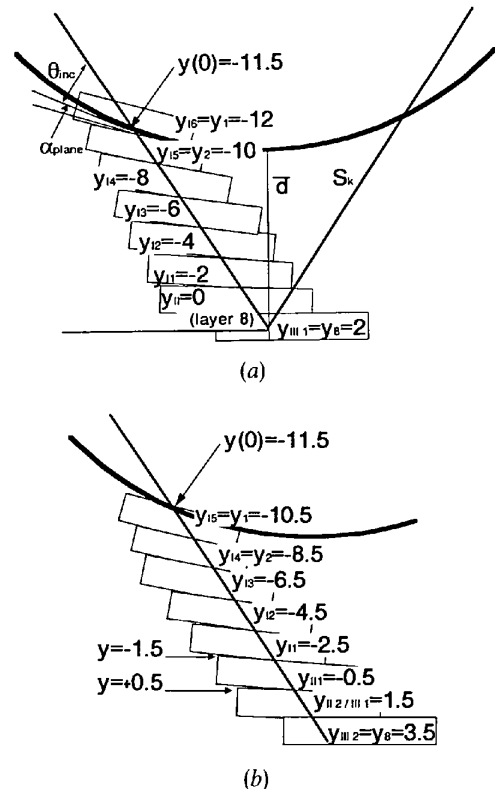


Fig. 3. (a) Use of prescription of Caciuffo *et al.* (1987), showing the discrepancy between the diffraction of the first layer and the corresponding crystal region, with periodicity  $dy = 2$  and amplitude given by the reflectivity of the first layer. A simple estimate of the depth penetration  $\bar{d}$  for the lowest layer (III 1 or 8) is illustrated. (b) Division of crystal into equal-thickness blocks, beginning at the surface: note that the peak of the Darwin curve ( $y = -1$  to  $+1$ ) is divided into two regions and interference between the two is neglected.

and transmitted intensity for the crystallite of thickness  $t_0$ , approximations in the thick-crystallite case could be  $r_1 = r_{t_0}$  and  $t_1 = t_{t_0}$ ; in the thin-crystallite extreme,

$$\begin{aligned} r_1 &\simeq r_{t_0}(t/t_0)^2, \\ t_1 &\simeq t_{t_0}^2, \end{aligned} \quad (8)$$

where  $t$  is the thickness of the first layer and  $t_0$  is the normal lamellar thickness. The latter is more appropriate to this problem but is only approximate. The interference problem is critical when  $y(0)$  is near 0, since this region diffracts most of the radiation if  $\Delta y = 2$ , especially if absorption is strong for the given radiation. Reducing the effective thickness of the first lamella may give errors of an order of magnitude in the reflectivities. Thus, this adaptation of the model also contributes large periodic error.

For many rays, most of the reflectivity will arise from the first layer. This is true if absorption is strong, if the diffraction coordinate  $y(0)$  is within or near the Darwin total reflection condition or if  $y(0)$  is greater than this value. Then the full layer thickness must be used, setting  $y \simeq y(0)$  for the first case,  $y(0) < y < y(0) + \Delta y$  for the second case and  $y \simeq y(0)$  for the third case. Each subsequent layer must then have  $y$  increased by the equivalent thickness of the crystallite  $\Delta y$ . When  $y(0) \ll 0$  with small absorption, peak reflectivity arises from the layer in which  $y \simeq 0$ . Here the first layer is of little significance and the original model may be followed for all subsequent layers ( $y = n\Delta y$ ) with the thickness and effective diffraction coordinate for the first layer chosen to complete the distance to the surface [ $y_1 \simeq y(0) - \Delta y_1/2, \dots$ ]. This prescription includes dominant effects to first order. Problems arise regarding continuity between these regimes, but there are more serious flaws in other aspects of the original model.

### 5. Depth penetration and focusing: a simple model

The simplest estimate of depth penetration is given by the difference between  $y_j$  and  $y(0)$  for component  $j$ . This is equivalent to a depth perpendicular to the surface

$$\bar{d} = (2Rz/\cos \alpha_1)[\cos \theta_{\text{inc}}/\cos(\theta - \alpha_{\text{plane}}) - 1], \quad (9)$$

where  $\theta = \theta_j$  is the angle to the relevant diffracting planes, given by

$$\begin{aligned} \alpha &= 2y_j C(|b|^{1/2}/b) |\psi'_H| - [(1-b)/b] \psi'_0 \\ &= 4 \sin \theta_B (\sin \theta_B - \sin \theta) \simeq 2(\theta_B - \theta) \sin 2\theta_B \end{aligned}$$

or

$$\begin{aligned} \theta &= \arcsin \{ \sin \theta_B - [C|b|^{1/2} |\psi'_H| / (2b \sin \theta_B)] y_j \\ &\quad + [(1-b)/b] \psi'_0 / (4 \sin \theta_B) \}. \end{aligned} \quad (10)$$

The path length from the crystal surface is then

$$\begin{aligned} S_{j,\text{in}} &= (2Rz/\cos \alpha_1 + \bar{d}) \sin(\theta - \alpha_{\text{plane}}) \\ &\quad - [(2Rz/\cos \alpha_1 + \bar{d})^2 \sin^2(\theta - \alpha_{\text{plane}}) \\ &\quad - 4Rz \bar{d} / \cos \alpha_1 - \bar{d}^2]^{1/2}. \end{aligned} \quad (11)$$

Similarly, the path length  $S_j$  from depth  $\bar{d}$  to the crystal surface is given from (11) by making the substitution

$$\theta - \alpha_{\text{plane}} \rightarrow \theta_r + \alpha_{\text{plane}} \quad (12)$$

where [replacing  $b$  with  $1/b$  in (10)]

$$\begin{aligned} \theta_r &= \arcsin \{ \sin \theta_B - [Cb |\psi'_H| / (2|b|^{1/2} \sin \theta_B)] y_j \\ &\quad + (b-1) \psi'_0 / (4 \sin \theta_B) \}. \end{aligned} \quad (13)$$

By correspondence with (9), the output angle is

$$\theta_{\text{out}} = \arccos [1 + (\bar{d} \cos \alpha_1 / 2Rz) \cos(\theta_r + \alpha_{\text{plane}})] \quad (14)$$

and  $\theta_{Az}$ , the shifted value of  $\theta_A$ , is

$$\theta_{Az} = \theta_A - \theta - \theta_r + \theta_{\text{inc}} + \theta_{\text{out}}. \quad (15)$$

The profile on the source-angle scale [ $P_H(\theta_s) / P_0^e(\theta_s)$ ] is dominated by the truncated Gaussian distribution, which does not appear on other scales, while the depth-penetration effect will only appear as a shift on the  $Y_{iz}$  (detector) scale; on other (angular) scales, the effect of possible diffraction from a deep layer will simply add to the total intensity. Equations (8.29)–(8.30) of CMRB (assumption VI) may be replaced by the above.

Defocusing and relaxation effects of the crystal may be modelled by introducing a Rowland-circle radius  $Rzf$  applying to the film location only, so  $2Rz$  for the crystal and diffraction may be varied from  $2Rzf$  to test the error introduced. Deviation from cocentricity of these two circles will primarily lie along the vector from the centre of the crystal to that of its circle, of magnitude  $Cx$ . Diffraction equations are unchanged, but relations for  $Y_{iz}$  at the film surface in terms of  $\theta_{Az}$  and  $\theta_2$  become

$$\begin{aligned} \text{xline} &= -b' + [b'^2 + 4Rz^2(\cos \theta_{Az} - 1.25) + Rzf^2 \\ &\quad - Cx^2 + 2RzCx(1 + 2 \cos \theta_{Az})]^{1/2}, \end{aligned} \quad (16)$$

$$-b' = 2Rz \sin \theta_2 - (Rz - Cx) \sin(\theta_2 - \theta_{Az}), \quad (17)$$

$$\begin{aligned} Y_{iz} &= Rzf \arccos [(2Rz/Rzf) \cos \theta_{Az} - Rz/Rzf \\ &\quad - (\text{xline}/Rzf) \sin(\theta_2 - \theta_{Az}) - Cx/Rzf]. \end{aligned} \quad (18)$$

### 6. Form factors and scattering

Henke, Lee, Tanaka, Shimabukuro & Fujikawa (1982) and Viegele (1973, 1974) have compiled tables of form factors and absorption coefficients in the X-ray region, used here to derive profiles and diffraction shifts. Elastic reflection of X-rays by the crystal surface is

governed by the Fresnel equations. Except for grazing-incidence geometry, roughly 0.01% of incident radiation will be reflected, giving a smooth and slowly varying background at the detector. This is incoherent with atomic scattering from the lattice and is neglected in all models. The standard interpolation formula for  $\mu_a$  follows the empirical relation

$$\mu(\omega) = \begin{cases} (\omega_k/\omega)^n \mu(\omega_k), & \omega > \omega_k, \\ 0, & \omega < \omega_k, \end{cases} \quad (19)$$

where  $\omega_k$  is the threshold frequency, with  $n \simeq 3$  fitted by adjacent data points. Interpolation for  $f_2$  proceeds in the same way, while a linear interpolation for  $f_1$  is adequate, providing values for the region governed by the tables. Interpolation fails at absorption edges, but gives a first-order estimate. Tables have been extrapolated to 0.10–20 keV, using the form of approach to the limit  $f_1 \rightarrow Z$  at high energies, yielding estimated errors of less than 1%. For high-order reflections, the non-point-like electron density of the atoms becomes significant and reflections are weakened by interference from the electron cloud.  $f_1$  is corrected for relativistic and angle-dependent factors by using  $f'_1 = f_1 - \Delta f_r - \Delta f_0$ ,

$$\begin{aligned} \Delta f_r &\simeq 5|E_{\text{tot}}|/(3mc^2) + (Z/2)(E/mc^2)^2 \\ &\simeq 2.19 \times 10^{-6}Z^3 + 1.03 \times 10^{-4}Z^2 \\ &\quad + 1.91 \times 10^{-6}Z[E(\text{keV})]^2 \end{aligned}$$

$$\text{or } \Delta f_r \simeq |E_{\text{tot}}|/(mc^2)$$

$$\Delta f_0 = Z - \int_0^{\infty} U(r)(\sin q'r)/q'r \, dr, \quad q' = 4\pi(\sin \theta)/\lambda \quad (20)$$

where  $E$  is the photon energy and  $U(r)$  is the radial charge distribution, with the analytic approximation to the integral taken from *International Tables for X-ray Crystallography* (1974).  $sp^3$  hybridization was assumed for C and Si form factors, while neutral-atom values were used for H, N, O, P, Al and K factors (where required). Minor discrepancies arise from valence-orbital bonding in particular crystals.

Thick perfect crystals with small radii of curvature have large strains, limited by bond strengths in the crystal structure. If these do not shatter or lead to shear dislocations and phase boundaries (and hence mosaic structure), the strain will distort unstressed form factors. This is only significant for valence electrons near the breaking strain and is assumed negligible in this as in all models. Additional effects of curvature on structure factors are assumed negligible, the largest being due to changes in  $2d$  spacing.

### 7. Assumptions in the derivation of structure factors

Thermal motion of atomic scatterers results in a smearing of the electron density function  $\rho(r)$  and a decline of the scattering amplitude (*International Tables for X-ray Crystallography*, 1983, §§2.5–2.6).

Here atoms are assumed to oscillate independently, so thermal diffuse scattering effects are negligible, giving

$$\begin{aligned} F(hkl) &= [I(\mathbf{K} = hkl)]^{1/2} \\ &= \sum_j f_j \exp(-M_j) \exp[2\pi i(hx_j + ky_j + lz_j)]. \end{aligned} \quad (21)$$

Near absorption edges (within 50 eV) this is false but if, as in the current case, the crystal sees a narrow (Gaussian) distribution of energies, mean values will average over fine structure to yield the above estimates. Mean thermal parameters have been applied from crystallographic determinations of structures of the diffracting crystals used. Error of mean thermal corrections for form factors are largest for higher-order reflections (and larger scattering angles), but are reduced by inclusion of structurally dependent bonding effects.

Empirical summation rules for absorption coefficients are given elsewhere (*International Tables for X-ray Crystallography*, 1983, §3.2). Coherent Rayleigh scattering and incoherent Compton scattering contributions to the loss of intensity and to experimental absorption coefficients are assumed small or uniform for measurements in the polycrystalline state. Summation rules for attenuation coefficients and interpolation formulae are valid to a few percent, so form factors and structure factors are also valid. Structure factors and  $\psi$  values are complex, providing absorptive and scattering components for the coherent interaction of photons with the crystal.

The total attenuation coefficient within the crystal is given by  $\mu_{\text{tot}} = \mu_{\text{photoabs}} + \sigma_{\text{coherent}} + \sigma_{\text{incoherent}}$ . Photoabsorption and coherent scattering are taken into account in the above equations and  $\mu_{\text{photoabs}}$  is given accurately by  $-(2\pi/\lambda) \text{Im}(\psi_0)$ . To arrive at the total attenuation in a region not diffracting at the Bragg angle, estimates of coherent and incoherent contributions must be added (Viegele, 1974). Incoherent scattering has absorptive and scattering components, but removes intensity from the beam, reduces the locally available number of oscillators and is absorptive. Scattered photons neither interfere with the field directly (to first order) nor couple to field equations *via* interaction with further oscillators. The incoherent cross section should thus be added to  $\text{Im}(\psi_0)$  and  $\text{Im}(\psi'_H)$ .

Previous developments of the theory (Zachariasen, 1945; James, 1963; Taupin, 1964; CMRB) have neglected or ignored this effect, although the first two discuss incoherent scattering. For hydrogen at 2 keV, the incoherent contribution is 14% of the total attenuation coefficient, while at 10 keV 93% of the total attenuation is provided by this process, including a 6.5% contribution from the coherent process (Viegele, 1973, 1974). The effect on the imaginary component

of  $\psi$  in this case is therefore to increase it by two orders of magnitude! (See Fig. 4.) For a typical hydrogenous diffracting crystal such as pentaerythritol ( $C_{10}H_{24}O_8$  called PET here), neglect of coherent and incoherent attenuation at 10 keV yields an error of 24% in the attenuation coefficient, while neglect of incoherent attenuation gives an error in calculated structure factors and  $\psi$  values of 12%. This affects calculated intensities and alters profile shapes and penetration depths of radiation into the crystal. For inorganic crystals of medium- $Z$  elements such as silicon, this effect is negligible at up to 20 keV but rapidly dominates at higher energies. At lower energies, it is significant for elements up to oxygen (2% change of  $\psi$  at 10 keV). Interpolation and derivational errors of form and structure factors lie at this level, so effects for elements with  $Z > 8$  may be neglected. Bonded hydrogen form factors are imprecise, enhancing corresponding errors, but incoherent contributions to these are not greatly affected by chemical bonding.

### 8. Finite flat perfect crystals

Constraints of available computing time require that the  $\theta_s$  and  $x$  loops are efficient. The greatest contribution to CPU time involves computation of finite flat crystal reflectivities and transmitted intensity ratios [ $r(\theta_{inc}), t(\theta_{inc})$ ] over the range of diffracting angles for  $\Delta y$ , the calculated layer thickness. This is conducted outside the above loops and used in the summation of reflectivity over  $\theta_s$ ,  $x$  and the crystal layers. The procedure allows finite flat-crystal profiles and results to be checked independently.

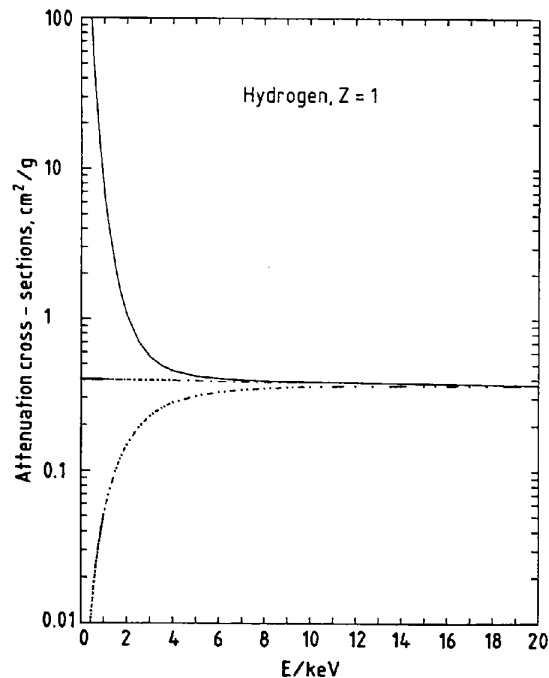
A discrepancy existed between calculations using the 'improved' expressions given in assumption VII and those using the original complex form. This difference may be partially due to different evaluation of circular functions, but is dominated by the correction of Wilkins (1978). Magnitudes of terms are correct, but the sign of the second term is often false (Wilkins, 1978; Suortti *et al.*, 1986).

In the face of this problem, 'unsimplified' formulae (Zachariasen, 1945) were used, avoiding errors or approximations introduced in further modification of the formulae. The power ratio of the diffracted wave at the incident surface is

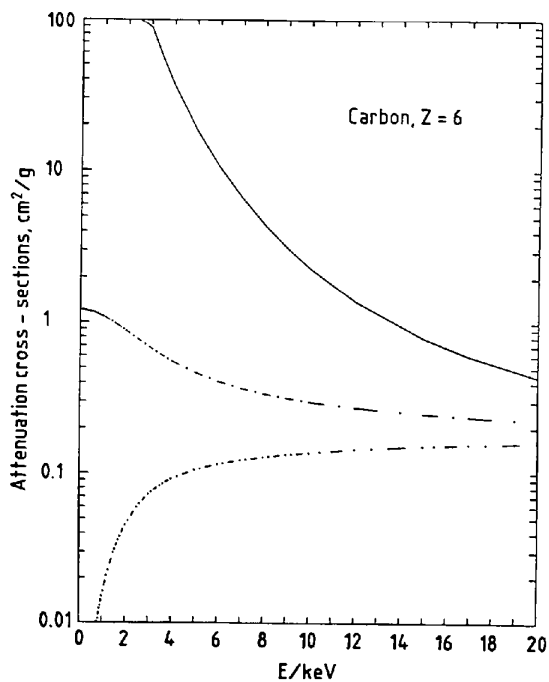
$$\frac{P_H}{P_0^e} = (1/|b|)(I_H/I_0^e) \\ = (1/|b|)|[x_-x_+(c_- - c_+)]/(c_-x_- - c_+x_+)|^2 \quad (22)$$

and that of the transmitted beam at the exit surface  $\mathbf{n} \cdot \mathbf{r} = t_0$  is

$$\frac{P_e^0}{P_0^e} = \frac{I_e^0}{I_0^e} = |[c_-c_+(x_- - x_+)]/(c_-x_- - c_+x_+)|^2 \quad (23)$$



(a)



(b)

Fig. 4. Attenuation cross sections for (a) hydrogen and (b) carbon, in  $\text{cm}^2 \text{g}^{-1}$ , versus photon energy from 0 to 20 keV. Upper curve (—) gives total attenuation cross section,  $\mu = \tau + \sigma_{\text{coherent}} + \sigma_{\text{incoherent}}$ ; the middle curve (---) gives the sum of scattering contributions, omitting photoabsorption, equal to  $\mu - \tau$ ; the lower curve (-·-·-) gives the incoherent scattering cross section omitted in previous applications of the theory.

with

$$c_{\pm} = \exp [(-2\pi i \delta_{0\pm})/(\lambda \gamma_0)] \quad (24)$$

$$\delta_{0\pm} = \frac{1}{2}[\psi_0 - z \pm (q + z^2)^{1/2}] \quad (25)$$

$$x_{\pm} = [-z \pm (q + z^2)^{1/2}]/(\psi_H C) \quad (26)$$

for the two internal incident waves and two internal diffracted waves ' $D_{0\pm}$ '. These formulae are as computationally efficient as the reduced version.

Erola *et al.* (1990) and Popovici *et al.* (1988) include the correction of Wilkins, showing qualitative agreement with integrated reflectivities. Experimental and calculated profiles show relatively poor agreement, especially in the Laue case. The Bragg case shows a profile broadening (and shift) of experiment compared with theoretical results, as would be expected from §11 below.

### 9. Assumptions of complex finite flat perfect crystal formulae

Zachariassen's (1945) derivation assumes that the diffracting crystal is a linear isotropic dielectric, so only applies approximately to crystals such as barium  $\beta$ -borate, calcite or aluminium. Corrected finite perfect crystal formulae involve assumptions that the incident wave is infinite and planar and that the crystal surface is planar. The plane-surface assumption is not theoretically valid for X-rays since wavelengths are equivalent to the atomic separation and the surface should be periodic in space around the nuclei and electron clouds (James, 1963; von Laue, 1949; Ewald, 1916). However, the simpler assumption represents an 'average' surface and results appear to agree with experiment.

A condition for the validity of the plane-wave approximation (that the angular width of a coherent incident wave at the surface be less than the angular width of reflection) is not satisfied. The latter is about  $10^{-5}$  rad while the former is commonly  $10^{-4}$  rad but in the case of the SS1 instrument used is about 0.1 rad. The entire range of diffracting angles (and wavelengths) is illuminated with coherent radiation and in principle interference is possible between all internal diffracting waves for each of these angles, the fields superposing in the crystal. Kato (1960) showed that wave bundles do not interfere, except for crystal regions close to the incident surface. Thus, *Pendellösung* interference phenomena relating to non-parallel diffraction vectors, which would occur in plane-wave theory, do not normally occur. Integrated intensities appear essentially identical for spherical- and plane-wave theories.

### 10. Application to PET 002

PET is a crystal often used in diffraction studies over the 1–7 Å range but deteriorates with age or strong

X-ray irradiation, is soft and readily deformed and should be stored in a desiccator (Burek, Barrus & Blake, 1974; Burek, 1976). It deforms plastically under stress, but has the advantage of a high integrated reflectivity. The crystallographic space group has been reported as  $I4$  (Eilerman & Rudman, 1979). There are 42 atoms (2 molecular units) in the unit cell. Lattice constants for this (tetragonal) space group have been reported as  $a = 6.10$  (1),  $c = 8.73$  (1) Å (Frolov, Vereshchagin & Rodionov, 1962).

This latter figure would imply a  $2d$  spacing for the (002) plane of 8.73 (1) Å, of low precision. Other evaluations of the spacing gave 8.742 Å (Burek, 1976) and

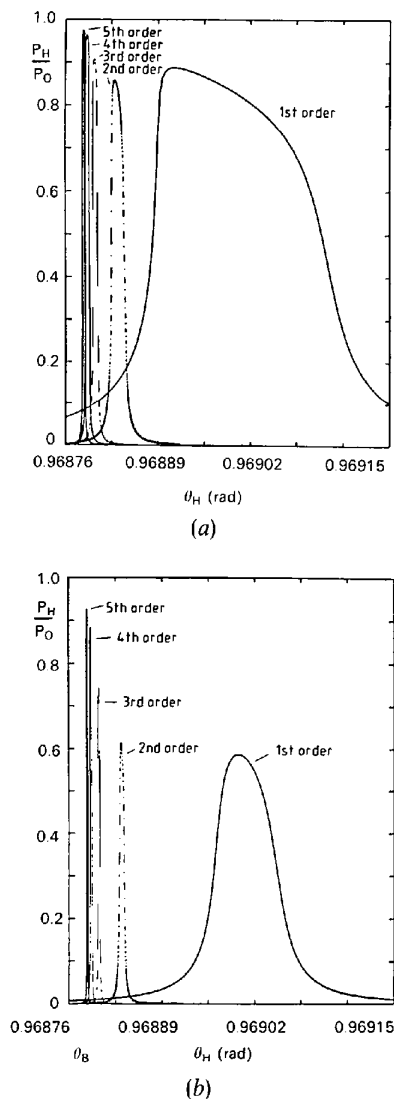


Fig. 5. Calculations using the equations of Cole & Stemple (1962) for infinite flat perfect crystals of PET 002 for various orders of diffraction for 7.2 Å/n, orders  $n = 1$  to 5, for (a)  $\pi$  polarization and (b)  $\sigma$  polarization.  $P_H/P_0$  vs  $\theta$ ,  $\theta_B = 0.968779$  rad using  $2d = 8.7358$  Å.

8.757 Å (Eilerman & Rudman, 1979); the latter provided atomic positions in the unit cell, enabling form factors and structure factors to be evaluated. Discrepancies between measurements could imply either that the degree of perfection and deterioration of typical PET crystals covers this range or that these results were of limited precision. This imprecision could give a large uncertainty in derived wavelengths.

A precise study has been made of the thermal expansion of the  $2d$  spacing for this plane (Hall, 1980) yielding the value of 8.7358 (6) Å at and near 291 K, which is inconsistent with the result of Eilerman & Rudman (1979) but consistent with other measurements. We take this as the true value and correct the lattice constant in the structure accordingly.

The particular crystals had tolerances quoted by the suppliers of  $0.40 + 0.05 - 0.02$  mm for the thickness and  $\pm 5''$  for the parallelism of the diffracting planes to the surface. These should be conservative estimates and may also be used as an upper limit on the mosaic angular spread. The thickness uncertainty will be seen to be significant in the subsequent article, including possible variation of thickness along the crystal.

Fig. 5 displays calculated profiles for infinite flat perfect PET 002 crystals diffracting in orders  $n = 1$  to 5 corresponding to 7.2 Å in the first order. They may be compared with finite flat perfect crystal calculations using (22)–(26) in Fig. 6, where the crystal thickness is defined by the curvature and  $\Delta y = 2$ . Similar results are obtained for  $\sigma$ -polarized radiation, with thicknesses (from  $\Delta y = 2$ ) of 59.8, 10.1, 8.74 and 6.69  $\mu\text{m}$  for orders  $n = 1$  to 4.

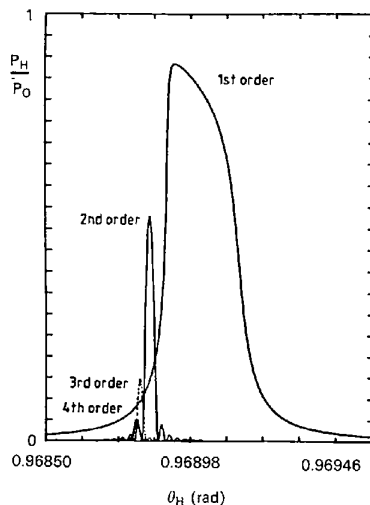


Fig. 6. Plot of  $P_H/P_0$  versus  $\theta$  from calculations for first- to fourth-order  $\pi$ -polarized radiation following (22)–(26) for finite flat perfect crystals of PET 002 corresponding to 7.2 Å for order one. Note the *Pendellösung* oscillations, especially in higher orders, in contrast with Fig. 5. Crystal thicknesses are 141, 12.2, 9.91 and 7.59  $\mu\text{m}$ , orders 1 to 4 (see text).

Deficiencies of models used previously for differential Lamb-shift measurements are detailed elsewhere (Chantler, 1990); they are dominated by problems in estimating curved-crystal depth-penetration shifts from infinite flat crystal calculations. No thermal parameters were used in the previous model since none were reported in the structural determination of Eilerman & Rudman (1979). Isotropic parameters for C, H and O atoms do not vary greatly between chemical species, so mean values of  $\beta_{11} = \beta_{22} = \beta_{33} = 0.0084$ ,  $\beta_{12} = \beta_{13} = \beta_{23} = 0.00$  for C, with  $B = 3.2$  and  $1.0 \text{ \AA}^2$  for O and H, should be accurate to 10% when used in

$$F(hkl, \text{room temperature}) = F(hkl, T = 0 \text{ K})f_\theta,$$

$$f_\theta = \exp[-B/(2d)^2] = \exp(-n^2 \sum \beta_i h_i h_j), \quad (27)$$

where  $h_{1,2,3}$  denote  $H, K, L$ ,  $2d$  denotes  $2d(002)/n$  and  $n$  is the order of 002 reflection used. This decreases intensities of higher-order reflections with respect to first-order diffraction (increasing depth penetration) and with respect to  $F_{000}$  (increasing the effect of incoherent attenuation).

## 11. Breakdown of the model

The finite flat (perfect) crystal profiles calculated prior to ray tracing are shown in Fig. 7 for the first three

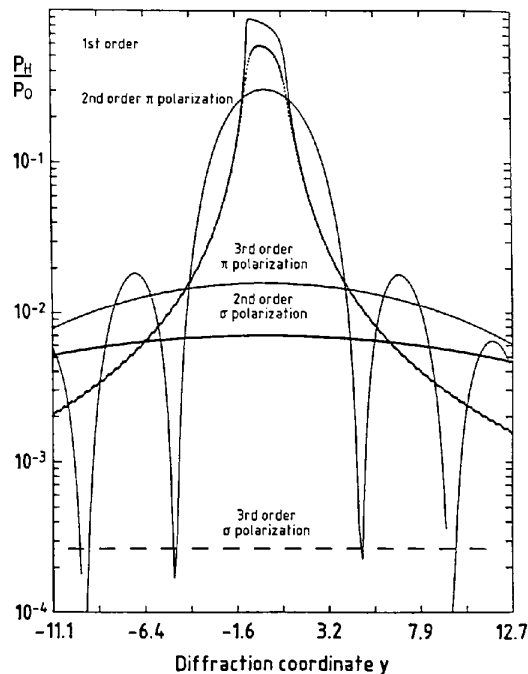


Fig. 7. Logarithmic plots of  $P_H/P_0$  versus diffraction coordinate  $y$  for finite flat perfect PET 002 crystals using a thickness corresponding to  $\Delta y = 2$  (following Caciuffo *et al.*, 1987) revealing that higher-order radiation involves large interference terms between such layers.

orders of diffraction from PET 002 in both polarizations. Profiles are plotted on the diffraction coordinate ( $y$ ) scale, calculated using layer widths corresponding to  $2Rz = 300$  mm. They show that profiles for different radiation and polarizations could vary in widths (FWHM) on the  $y$  scale from  $\Gamma(y) = 2$  to 433! In addition, these values corresponded to layer thicknesses from 3.7 to 140  $\mu\text{m}$ . It is therefore clear that several assumptions of the above model are false.

If the curvature  $c \propto 1/R$  is large, each layer for  $\Delta y = 2$  will be very thin, so only a small amount of diffraction will occur from each crystallite. There will be relatively few atomic layers providing the interference for the sharp 'Darwinian' profile edges, so that for all crystals diffraction will occur over a wider range of angles. Effective layer thicknesses arise from the relative importance of absorption of different polarizations for the same  $\Delta y$ , the range being  $t_0 \approx 2Rz [\Gamma(y)C|b|^{1/2}|\psi'_H|/(b \sin 2\theta_B)]^2$ . In the case of PET 002 diffraction, first-order lines show  $\Gamma(y) \sim 2.5$  but third- and fourth-order lines show  $\Gamma(y) \sim 12$  to 100. This is consistent with the curvature for the third-order lines being of the order of 60, fourth-order lines having  $c \sim 48$  to 170 ('strongly bent') while that for first-order lines is 0.11 to 0.0285 ('near perfect') for the same bending radius ( $2Rz = 300$  mm) (cf. CMRB).

Thus, the assumption of  $\Delta y = 2$  to account for interference effects is false, so a thicker layer must be used and the assumption that  $y$  is single-valued for a given layer is also false (regarding both diffracted intensity and depth penetration).

## 12. A new model

The source parameters of §§3 and 5 remain as described above. Any other source geometry may replace that given therein. The main features of the model in §2 are corrected and given as the following (see Fig. 8).

(I) A curved crystal is considered to be oriented with respect to a monochromatic incident-beam element from the source so that the deviation from the  $y = 0$  diffraction 'peak' at the crystal surface is  $y(0)$ . The curved crystal is divided into crystallites or lamellae of equivalent thickness  $\Delta y_0$ , where  $\Delta y_0$  also corresponds to the width of the diffraction curve  $\Gamma(y)$  for the flat crystallite.

(II) The condition  $-\Delta y_0/2 < y < +\Delta y_0/2$  defines the range of the flat crystallite diffraction peak, including finite thickness and order effects. This region (region 2) corresponds to a volume of the curved crystal in which coherent diffraction from different parts of the crystallite is significant. It is less sharply defined than in the earlier model, but may be assumed to diffract X-rays as a perfect crystal of this thickness, having the orientation of some middle plane – that is,  $-\Delta y_0/2 < y < +\Delta y_0/2$ .

(III) Regions 1 and 3 are considered as an ensemble of perfect crystals, each having a thickness corresponding to  $\Delta y = \Delta y_0$  and a misorientation  $\Delta y_0$  with respect to its neighbour. The midplanes of each crystallite maintain the same orientation as in the real crystal, but so must the other values of  $y$  providing contributions to the reflectivity in the crystallite. By analogy with §§2 and 4, the model is not composed of mosaic blocks (it is not a model of imperfect crystals of finite thickness and angular misorientation distribution), nor is it composed of a mean of blocks projecting from or into the surface (the surface is assumed to be planar and atomically perfect). It is also not composed of a mean of half-sized blocks and subblocks filling the 'gap' to the surface (problems of absorption and scaling), nor is it composed of several

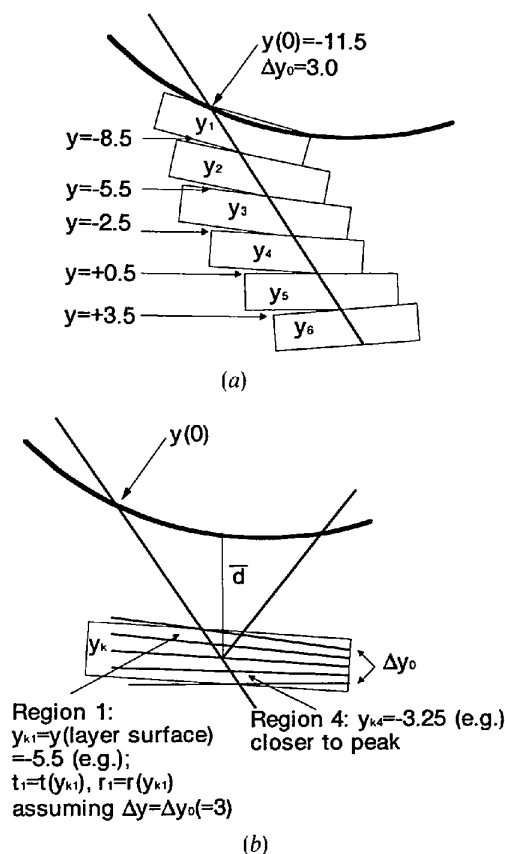


Fig. 8. (a) New model, showing separation of crystal into curved lamellae of equal thickness  $\Delta y_0$  with continuity from the surface.  $y_j, r_j, t_j$  and the depth penetration for each layer are given by (b) and in the text. The Darwin curve ( $|y| < 1$ ) and the dominant contribution to diffraction (arising from  $|y| < 1.5$ ) are split between layers 4 and 5. (b) Division of the lamellar unit into four regions for the calculation of the mean values of  $y, r, t$  and  $d$ . Each region is  $\Delta y = \Delta y_0/4$  in thickness, with  $r_i, t_i$  calculated using  $\Delta y = \Delta y_0$  to include interference from adjacent regions and weighted as given in the text. Diffraction in the layer shown is dominated (in the low-absorption limit) by the fourth region, yielding a relatively large mean penetration depth.

different regimes where various layers or processes are dominant (the suggested model of §4, suffering from continuity problems).

Instead, the model represents the crystal as composed of lamellae of finite curved crystallites so that, wherever diffraction occurs in the crystallite, the location of relevant planes will agree with those of the real (perfect) crystal. Each crystallite has the thickness on the diffraction coordinate scale as given above and the surface layer varies from  $y = y(0)$  to  $y = y(0) + \Delta y_0$ . At the peak this may neglect some interference effects but, in all cases and especially at the surface, the thickness and location of layers follows that of the crystal. Much of this omission is redressed in (VIII) below.

(IIIa) Reflectivity and transmission ratios of the finite curved crystallite are given by those of the equivalent flat crystallite. Lattice positions will be deformed from their unstressed values and form factors are restricted and directed by this curvature. The consequent change of  $2d$  spacing is primarily tangential to the surface and of maximum magnitude  $-T/(4Rz)$  at the surface (being equal and opposite at the rear face). A naïve estimate of the corresponding elongation of spacing normal to the surface (to reduce the apparent density increase) would be the square of this fraction. For a typical crystal thickness of 0.1 to 0.6 mm and  $2Rz$  value as low as 300 mm, this  $2d$  correction lies below the 1 part in  $10^6$  level (less than the uncertainty from a fluctuation of 1 K and less than most quoted lattice-spacing uncertainties). Mosaic crystals, with introduced dislocations and phase boundaries to reduce the stress, have even smaller shifts.

Use of flat-crystal formulae neglects the smooth continuous change of phase through the crystallite. This is given from (11) where  $\bar{d}$  is replaced by  $d_0$  (the minimum of the lamellar thickness and the mean penetration depth) and the path length is compared to  $S_{j,\text{flat}} = d_0/\sin(\theta - \alpha_{\text{plane}})$ . The phase of internal waves across the unit changes from that for a flat crystal by approximately

$$\begin{aligned} \Delta\varphi &= 2\pi d_0^2 / [(2Rz + t_0)\lambda \sin(\theta - \alpha_{\text{plane}})] \\ &\quad \times [1/\sin^2(\theta - \alpha_{\text{plane}}) - \frac{1}{2}] \\ &\simeq 4\pi d_0^2 / (2Rz \lambda), \end{aligned} \quad (28)$$

where the latter approximation holds to a factor of 2 for  $\theta > 36^\circ$  (i.e. for most of the range of the current spectrometer). For  $2Rz = 300$  mm,  $\lambda \simeq 7.1$  Å and  $d_0 \simeq 1$  μm, the phase change through the diffracting region is negligible. For higher-order radiation (in general), the phase shift rises to  $2\pi$  (e.g. for  $\lambda \simeq 1.78$  Å and  $d_0 \simeq 7$  μm). This supports the assumption of incoherence between lamellae, although interference terms in a lamella from the curvature may approach significance in some cases.

The phase change is significant for strong curvatures where, however, real thicknesses  $t_0$  are much reduced and the reflectivity profile is low, smooth and wide. Locations of *Pendellösung* peaks may shift slightly but the effect on all reflectivities should be small. So long as the crystal curvature is small compared with the scale necessary to superpose wave fields, the deviation from the true periodicity is small.

(IV) The reflectivity of the set of monocrystalline lamellae so obtained may be calculated from the energy balance as discussed in §2, but with layers of thickness given by  $\Delta y_0$  with diffraction coordinate  $y$  given as discussed in (VIII).

(V) Owing to the curvature and the 'sharp' drop of reflectivity outside the  $-\Delta y/2 < y < \Delta y/2$  region, multiple diffraction is neglected, since adjacent crystallite wave fields are incoherent and reflectivity outside region 2 is negligible. Therefore, layers may be treated independently and the diffracted power from the surface may be given by (1), where  $S_j$  is now given by (12).

Profile tails are affected by the assumed non-interference between lamellae adjacent to the peak diffracting unit but dominant contributions to the peak and 10th–90th percentile regions are given to high accuracy. Mosaic phase shifts from dislocations *etc.* yield the model exactly by eliminating coherence between crystallites.

(VI) For a given surface (or first-layer) orientation  $y(0)$ , the orientation of the surface of the  $j$ th layer  $y_j$  is given by

$$y = y(0) + (j - 1)\Delta y_0 \quad (29)$$

and depth penetration *etc.* to this surface is as given in §4.

(VII) For a given orientation  $y_{j,i}$  and thickness  $A_j$  of the  $i$ th element of the  $j$ th layer, it is assumed that the reflectivity and ratio of transmitted to incident powers for the layer  $j$  is given by general  $G$ -floating-format double-precision complex finite-crystal formulae [(22)–(26)]. These equations give an estimate of the X-ray diffraction pattern  $R = R[y(0)]$  for the curved crystal.

(VIII) The crystallite may yield a large uncertainty in evaluation of depth penetration and reflectivities owing to variation of  $r$  and  $t$  with  $y$  when either the crystallite thickness is macroscopic ( $t_0 \gtrsim 30$  μm) or when there is a large variation of  $y$  from the front to the rear surface of the crystallite. When  $y(0) \ll -\Delta y_0$  and absorption is small, reflectivity arising from the rear of the crystallite may be several orders of magnitude larger than that from the front surface and may give a corresponding depth shift. For  $y(0) \gg \Delta y_0$ , the front surface will be dominant by up to several orders of magnitude. Near the peak, estimates should relate to the peak height and FWHM of the curve

and not to front or rear surfaces (which may have 10% of the peak reflectivity).

A given depth in the curved crystallite is here assumed to contribute a reflectivity (at the crystallite surface) equivalent to a finite flat crystal of the crystallite thickness, multiplied by the square of the transmission loss to that depth. The estimate of transmission loss is precise, since transmitted power ratios are smooth functions. Reflectivities do not scale unambiguously with thickness but absorption, incoherent scattering and diffracted transmission all scale appropriately to first order. The square of the transmission loss is required [*versus*  $t \exp(-\mu S_j)$ ], since interference still occurs in this region for the diffracted beam. The use of the full thickness in this estimate includes most interference effects from adjacent regions above and below the given depth and hence redresses the neglect of interference from adjacent crystallites. This estimate may be justified by consideration of particular extremes, as discussed elsewhere (Chantler, 1990).

Summation over four depth elements, with  $y_1 = y_{\text{surface of layer}}$ ,  $y_2 = y_1 + \Delta y_0/4$ , ..., and  $r_i$  and  $t_i$ , the values for the flat crystallite of thickness  $\Delta y_0$ , yields mean values of crystallite reflectivity  $\bar{r}$ , transmission ratio  $\bar{t}$  and diffraction coordinate  $\bar{y}$  given by

$$\begin{aligned} \bar{t} &= \prod_{i=0}^n t_i^{1/n}, \quad \bar{r} = \sum_{i=0}^n r_i w_i / \sum_{i=0}^n w_i, \\ \bar{y} &= \sum_{i=0}^n y_i w_i / \sum_{i=0}^n w_i, \quad w_i = \prod_{j=0}^{i-1} t_j^{2/n}, \end{aligned} \quad (30)$$

where  $n = 4$ . The difference between  $\bar{y}$  and  $y_1$  then provides an additional depth shift, while the reflectivity and transmission for the crystal are derived using (IV) and (V).

The value of  $\bar{d}$  derived on this basis is insufficiently precise for many first-order lines. Large absorption leads to only the first layer contributing to the reflectivity. Further, this layer is commonly macroscopic (up to  $t_0 = 200 \mu\text{m}$ ) even if  $\Delta y = 2$  for the crystallite, so division of the layer into only four elements yields an uncertainty in  $\bar{d}$  commonly  $\sim \pm t_0/20$ , if averaging is accurate to 20% of the depth difference between adjacent regions. This uncertainty must be reduced by increasing the number of regions involved. Layers where  $j > 2$  and  $|y_j| > 5\Delta y_0$  contribute several orders of magnitude less intensity than the peak regions and are ignored. A cut-off where all slices  $x$  of the source have contributed their peak reflectivities is also imposed.

Details of the computation of finite crystallite profiles to convergence of precision and of resulting diffraction widths  $\Gamma(y)$  with  $\Delta y_0$  finite crystallite values are given elsewhere (Chantler, 1990). The asymmetry parameter  $b$  is recalculated from (6) for each angle  $\theta_{\text{inc}}$ , from which the equivalent thickness  $t_0$  for the given  $\Delta y$  (initially equal to 2) may be calculated.

Equations (22)–(26) are used to generate  $r(\theta)$  and  $t(\theta)$  over the resulting range of  $\theta$  and  $\Delta y$ , with additional values beyond this range computed for

$$\theta_{\text{inc}(i=1-10)} = \left\{ \begin{array}{l} \theta_{\text{min}f} \\ \theta_{\text{max}f} \end{array} \right\} \mp 2^{(i-2)/2} (\theta_{\text{max}f} - \theta_{\text{min}f}). \quad (31)$$

In the main calculation, for given  $\theta_s$ ,  $x$  and crystallite layer, there will be from 1 to 60 regions (or depths) defined for the crystallite, each of which will define a given  $y_i$  and  $\theta_i$  for the grazing-incidence angle to the ideal crystallite. If any value of  $\theta_i$  lies outside the range of the flat-crystal profile, limiting values are used:

$$\begin{aligned} r_i &= r \left( \left\{ \begin{array}{l} \theta_{\text{max}f} \\ \theta_{\text{min}f} \end{array} \right\} \pm 16 (\theta_{\text{max}f} - \theta_{\text{min}f}) \right) \simeq 0, \\ t_i &= t \left( \left\{ \begin{array}{l} \theta_{\text{max}f} \\ \theta_{\text{min}f} \end{array} \right\} \pm 16 (\theta_{\text{max}f} - \theta_{\text{min}f}) \right) \simeq 1. \end{aligned} \quad (32)$$

### 13. An example

For 7.2 Å/ $n$  radiation diffracting from PET 002 crystal planes in  $n$ th order,  $n = 1$  to 5, with a crystal radius of  $2Rz = 300 \text{ mm}$ ,  $\sigma$  polarization yielded mean penetration depths of 1.44, 30.6, 94.4, 150 and  $174 \mu\text{m}$  (Fig. 9) compared with the thicknesses of Fig. 6 and 7.  $\pi$  polarization gave mean values of 0.896, 28.1, 93.5, 150 and  $174 \mu\text{m}$ .  $\Delta y_0$  finite crystallite widths may be compared with resulting diffraction widths  $\Gamma(y)$  on the plot. All higher-order radiation was limited by the crystal thickness and gave adequate precision after division of each layer into four regions. These mean depths approach the zero-absorption limit of  $200 \mu\text{m}$  for high order,  $n \rightarrow \infty$ . First-order radiation after a depth of  $92.7 \mu\text{m}$  was  $1.4 \times 10^{-13}$  times the surface intensity. Hence, the surface layer dominates, requiring 38 and 60 regions ( $\sigma, \pi$ ) for adequate precision.

These wavelengths correspond roughly to the Doppler-shifted Lyman  $\alpha$ -Balmer  $\beta$  region in  $\text{Fe}^{25+}$ . The trend of  $\Delta y_0$  and  $t_0$  with diffracting order is consistent for all iron lines computed for PET 002 crystals, but the number of regions, mean depths, profiles and peak reflectivities vary considerably. For third-order Lyman  $\alpha$  radiation (Doppler-shifted  $\lambda = 1.7947 \text{ \AA}$ ,  $\theta_B = 38^\circ$ ), the crystallite thickness for  $\sigma$  polarization is  $4.82 \mu\text{m}$ , corresponding to  $\Delta y_0 = 56.9$ , with a mean depth of  $135 \mu\text{m}$  using four regions; first-order radiation at  $\lambda = 5.4305 \text{ \AA}$ ,  $\theta_B = 38.4^\circ$  gives crystallite thicknesses of  $8.37 \mu\text{m}$ , corresponding to  $\Delta y_0 = 2.43$ , and  $43.3 \mu\text{m}$ , corresponding to  $\Delta y_0 = 2.85$  ( $\sigma, \pi$ ), with mean depths of 4.89 and  $5.21 \mu\text{m}$  requiring 4 and 17 regions, respectively.

### 14. Allowance for photographic detection

Laming (1988) has explained the shift of peak location on photographic emulsions due to emulsion penetration by the radiation, which is energy dependent. The

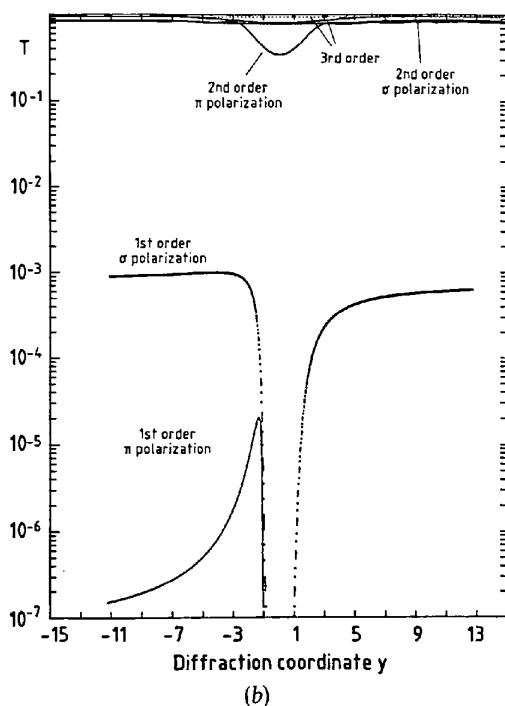
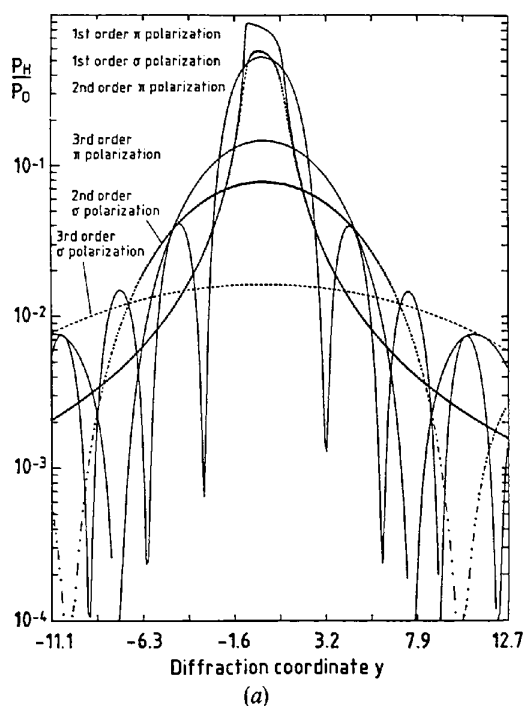


Fig. 9. Logarithmic plots of (a)  $P_H/P_0$  and (b)  $T$  versus diffraction coordinate  $y$  for finite flat perfect PET 002 crystals using thicknesses following §12, as given in Fig. 6; cf. Fig. 7. Lamellar  $\Delta y_0$  effective thicknesses for orders  $n = 1$  to 4 are 3.24, 7.49, 19.8, 27.6 ( $\sigma$ ) and 2.73, 3.23, 8.08 and 11.2 ( $\pi$ ) in agreement with diffraction FWHM  $\Gamma(y)$  to 10%.

geometrical equations referred to in §§3 and 5 define the location  $Y_{iz}$  and incident angle of radiation on the Rowland circle (*i.e.* on the emulsion surface). If electronic detection normal to the incident angle was used, the detector function would be symmetric and yield no additional shift. In our case, with a front emulsion thickness of  $13 \mu\text{m}$  and absorption and scattering coefficients given by the incident energy and composition of the emulsion (AgBr + gelatin), the detector function is an asymmetrical exponential. This is depicted in Fig. 10 and leads to a larger shift for higher-order radiation, calculated from

$$\Delta Y_{iz} = \int_0^{t_{\text{emulsion}}/\sin \theta} z \exp(-\mu z) dz \cos \theta \times \left[ \int_0^{t_{\text{emulsion}}/\sin \theta} \exp(-\mu z) dz \right]^{-1}. \quad (33)$$

For Fe Lyman  $\alpha_1$  radiation, Doppler-shifted ( $\beta \approx 0.136$ ) and diffracted in fourth order ( $\theta_B \approx 55^\circ$ ) by PET 002, this shift is  $3.55 \mu\text{m}$  for  $\mu_{\text{film}} = 0.062 \mu\text{m}^{-1}$  and a crystal radius of  $2 R_z = 300 \text{ mm}$ ; for Balmer  $\beta$  in first order, the shift is  $0.656 \mu\text{m}$  with  $\mu_{\text{film}} = 0.832 \mu\text{m}^{-1}$ . These values are doubled for the third-order Lyman  $\alpha$  region ( $\theta_B \approx 38^\circ$ ) and larger for the germanium Lyman  $\alpha$  experiment. They are small but important effects.

### 15. Method for testing; selected perfect-crystal profiles

The complex nature of the above equations, explicit mathematical assumptions and finite-element summations require testing. This is partially achieved by mental calculations. Results for infinite flat perfect crystals using corrected formulae may be compared with standard references (Zachariasen, 1945; CMRB), as well as with finite flat or curved perfect crystal parameters and profiles.

Control parameters allow calculation of infinite flat perfect crystal profiles, finite curved perfect crystal

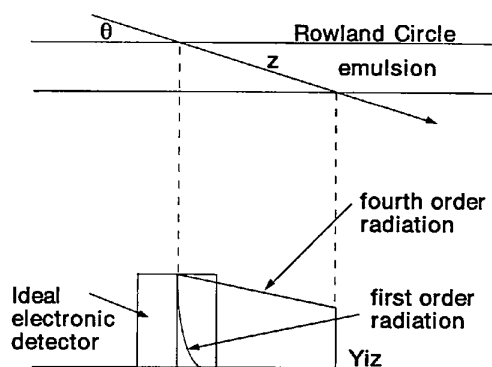


Fig. 10. Schematic diagram for photographic depth penetration and detector responses.

values or finite curved imperfect crystal results (see paper II), with or without the photographic-detector response for Kodak DEF film. Profiles with respect to source angle ( $\theta_s^{\text{rad}}$ ), grazing output surface angle ( $\theta_z^{\text{rad}}$ ) and detector location on the Rowland circle ( $Y_{iz}$   $\mu\text{m}$ ) are calculated for each polarization; also included are surface values  $y(0)(\theta_s)$  and dominant layer contributions  $y_j(\text{max})(\theta_2)$ ,  $y_j(\text{max})(Y_{iz})$ .

Four tests of theory and programming have been implemented (Fig. 11). One sets the number of steps over the source width  $x$  equal to one (treating the diffraction as arising from a point source) and sets the number of crystal layers for each  $\theta_s$  and for  $x = 0$  as one. This tests geometric focusing and defocusing and interpolation and finite-precision routines for  $\theta_s$ . The second uses a point source ( $x = 0$ , only a single step)

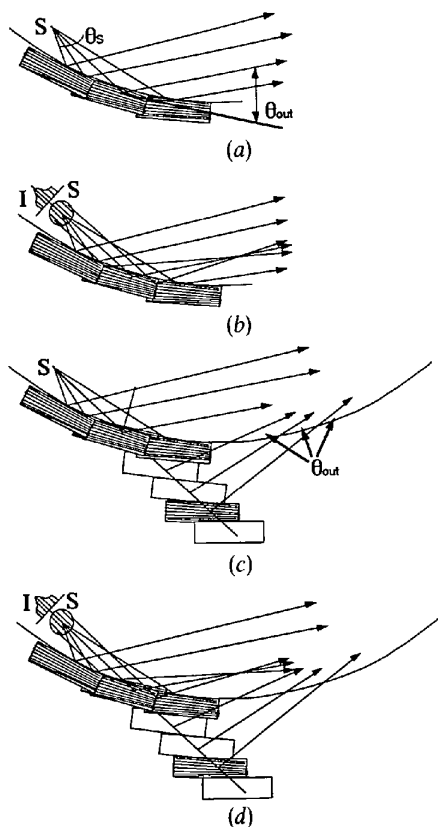


Fig. 11. Testing procedure for implementation, precision, continuity and shape of profiles. (a) Focusing, interpolation and finite precision tests with a point source looping over angle of emission ( $\theta_s$ ) and interacting with the surface layer only. Output profile scales are labelled. (b) More complete focusing and geometry tests using the finite-source distribution but interacting with the surface layer only. (c) Use of a point source but treating all diffracting layers, comparable to earlier models. Deeper layers for a given incident ray have the same  $\theta_{\text{out}}$  value but do not yield the same arc lengths  $Y_{iz}$  relative to the crystal pole. (d) Looping over the source location  $x$ , the emission angle  $\theta_s$ , the number of diffracting layers (curved crystallites or mosaic blocks) and the number of regions in each layer.

but treats all layers and may be compared with earlier curved-crystal models (CMRB) and with flat perfect crystal calculations. The third treats all steps of the Gaussian source width but only the surface diffraction layer, providing a more complete focusing and geometry test. The final profile loops over full ranges, giving diffraction and focusing results relevant to our study.

The standard example has been diffraction off  $2Rz = 300$  mm PET 002 $n$  crystals of  $7.2 \text{ \AA}/n$ ,  $n = 1$  to 4; plots of corresponding perfect-crystal profiles are given in Figs. 12 and 13. Unlike infinite crystals, there are additional effects, leading to *Pendellösung* oscillations. Unlike finite flat crystal profiles, the full depth of the crystal does not contribute equally to diffraction. Unlike mosaic crystals, the block size depends on curvature and the rate of change of beam angle to the lattice; the orientation of lamellae is also well defined.

Curved-crystal profiles are generally asymmetric and not centred on  $y(0) = 0$ , even when equivalent flat-crystal profiles are symmetric. Reflectivity is dominated by that of the first layer for  $y(0) > +1$  since  $y_j$  increases with depth, away from the diffraction peak. Conversely,  $y(0) < -1$  has a large  $r_j$  reflectivity for the layer where  $y_j \equiv 0$ . Thus, multiple layers may contribute and asymmetric contributions from deeper layers of the crystal follow a roughly exponential decline.

Results display expected effects of geometric defocusing, depth penetration, finite source widths and finite precision on profiles versus  $\theta_s$ ,  $\theta_2$ ,  $Y_{iz}$ ,  $y(0)$  and  $y_1$ , and the linearity (or otherwise) of the last two parameters compared with the first three. Crystal curvature often yields the dominant contribution to depth penetration, which is the main broadening and diffraction correction for higher-order radiation. Final profiles on the  $\theta_2$  scale indicate the effect of finite precision in the ray-tracing exercise (Fig. 12). With Johann mounting, the finite source has a significant qualitative effect, while the effect of finite precision, observable in some profiles, is small (Fig. 13). The range of profile asymmetry, width and diffraction shift with order and polarization is indicated by Fig. 13(d) for the current geometry, compared with Figs. 13(b), (c) for a point source.

Plots of scaled reflectivity against the  $y$  coordinate at the crystal surface (Fig. 14) allow comparison of profile tails and *Pendellösung* oscillations with the literature. The finite source and precision lead to sawtooth oscillations as the dominant diffracting lamella shifts to deeper layers. This is clarified in Fig. 15, where the  $y$  coordinate used relates to the lamella giving the dominant reflectivity component for a given  $Y_{iz}$  location. For the monotonic behaviour of point-source surface-layer diffraction, these plots are smooth well defined functions (*cf.* Fig. 9a). This

remains true for first-order profiles in Fig. 15, but second and deeper layers are dominant for certain regions of  $R'(Y_{iz})$  — namely when  $y(0) \ll 0$ . Point-source calculations demonstrate *Pendellösung* oscillations with no observable precision limitation.

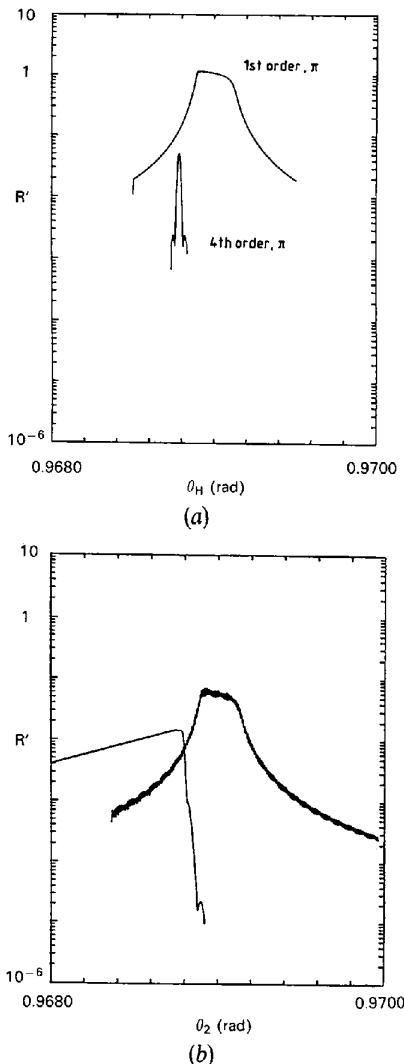


Fig. 12. Finite curved perfect crystal profiles for PET 002n,  $7.2 \text{ \AA}/n$ ,  $n = 1$  to  $4$ ,  $\pi$  polarization,  $2Rz = 300 \text{ mm}$ : Reflectivity versus (generatrix) exit angle at the crystal surface  $\theta_2$ . This is similar to plots versus incident (Bragg) angle. (a) Point-source surface-layer test showing narrow profiles, *Pendellösung* oscillations and similarity to flat-crystal profiles. (b) Finite-source multilayer profile. Profiles have large imprecision in finite-source single-layer tests, much improved for higher orders by inclusion of multiple layers. Asymmetry of profile tails is due to asymmetry of corresponding point-source profiles. Point-source single-layer results shown integrated reflectivities for higher orders increased dramatically by reflection from individual deep layers, and *Pendellösung* oscillations unaffected by precision. Rays are focused towards the peak, so peak values are greater than 1; the vertical axis is not reflectivity (it should be normalized by the result for a perfect X-ray mirror to yield reflectivities). The finite source induces no broadening, but adds a precision-based 15% oscillation for first-order radiation. Results for  $\sigma$  polarization are analogous.

Profiles plotted against  $\theta_2$  and  $Y_{iz}$  correspond to source emission of 2000 steps of height unity emitted into the covered angle. They thus correspond to the number and location of photons focused, for a total source strength of  $4000\pi/\Delta\theta_s$  photons in  $2\pi$ , where  $\Delta\theta_s$  is the covered source angular range. For the absolute source intensity distribution from the photon flux on the film, the solid angle involved may be derived from the path length  $BXYZF = BX + S_k + S_{kin} + xline$  to the emulsion from the mean source position. This gives  $Y_{iz}(\theta_{inc}, \theta_A, 2Rz, Rz, Cx, \alpha_1)$ . The first two parameters, together with  $BX$ , are fixed by geometric relations between spectrometer parameters (Chantler, 1990). Profiles corresponding to previous theoretical derivations are shown in Fig. 14, a plot of  $R$  versus  $y(0)$  from the  $\theta_2$  profiles, and, in Fig. 12, a plot of  $R$  versus  $\theta_2$ . Previous derivations neglect finite-source convolutions. Profiles including this and corresponding to observed spectra are given by Fig. 13(d).

Profiles show the same qualitative behaviour as earlier references which, however, omit corrections given above and cannot be directly compared to (real) profiles with a finite source. Other angles and orders display behaviour in qualitative consonance with ranges presented in CMRB. This does not imply adequate precision and formulation for other lines for which diffraction corrections are required. In calculation of corrections for all in-beam source-calibration lines, first-, third- and fourth-order reflection profiles were plotted and considered in detail at the third-order Lyman  $\alpha$  region, and first-, fourth- and fifth-order reflections near the Lyman  $\alpha$  and Balmer  $\beta$  regions were considered. This covers extremes of the region densitized on the film. Lines near  $45^\circ$  were also tested.

## 16. Output parameters and example values for PET 002, 008

Output files list wavelengths, integrated reflectivities  $R$  and refractive-index shifts for each polarization in terms of either  $C_{Y_{iz}} = \bar{Y}_{iz} - Y_{iz,0}$  or  $C_\theta = 1 - n\lambda/(2d \sin \theta'_{inc})$ . Here,  $Y_{iz,0}$  is the film-surface location corresponding to a point-source Bragg-angle diffraction from the crystal surface ( $\theta_{out} = \theta_r = \theta = \theta_{inc}$ ) and  $\theta'_{inc}$  is the value of  $\theta_{inc}$  expected if a point-source crystal-surface Bragg-angle reflection led to the value of  $\bar{Y}_{iz}$ . Both values include refractive-index corrections and depth-penetration corrections, but neither allows for the diffracting region lying off the Rowland circle, calculated separately and implicitly.

Representative results are given in Table 1 for  $\text{Fe}^{25+}$  ( $\beta = 0.136$ ,  $\alpha_{plane} = 0$ ) Balmer  $\beta_4$   $2s-4p_{1/2}$ ,  $\lambda_{rest} = 7.10054 \text{ \AA}$  with Doppler-shifted  $\lambda_D = 7.1671 \text{ \AA}$ ,  $\theta_B = 0.96217 \text{ rad}$ , and Lyman  $\alpha_1$   $1s-2p_{3/2}$ ,  $\lambda_{rest} = 1.77802 \text{ \AA}$ ,  $\lambda_D = 1.79469 \text{ \AA}$ ,  $\theta_B = 0.964500 \text{ rad}$ , diffracted in first and fourth orders from  $0.4 \text{ mm}$  thick

perfect PET 002 crystals.  $2Rz = 300$  mm and  $s_w = 1$  mm are assumed, together with typical parameters defining the source location. Scales given correspond to the four output profiles ( $\theta_s, \theta_2, Y_{iz}$  for the curved crystal and  $\theta_{inc}$  for the finite flat crystal). The  $Y_{iz}$  scale

is given relative to the point-source surface-Bragg-angle reflection, so indicates diffraction shifts.

Smoothness and consistency of profiles is checked from output ranges, quartiles and peak locations. Errors in ranges or approximations could be large for

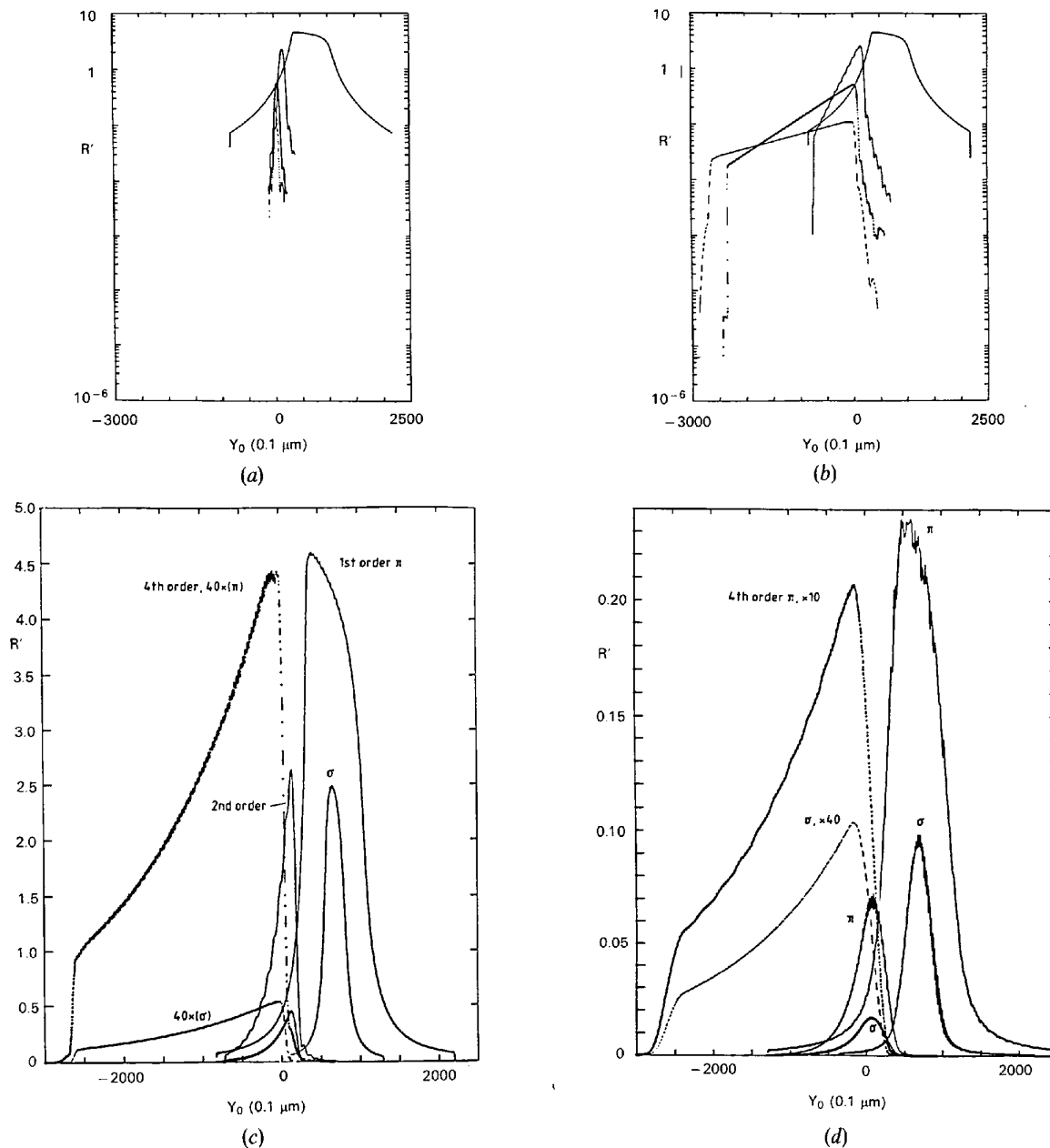


Fig. 13. As Fig. 12 but profiles are plotted against  $Y_{iz}$  relative to the value for point-source surface Bragg reflection. Profiles show diffraction shifts by the discrepancy from  $Y_0 = 0$ . (a) Point-source single-layer test, dominated by first-order profile and shift, showing the focusing of the Rowland circle (and the continuity of the calculation);  $\pi$  polarization,  $n = 1$  to 4 plotted. (b) Point-source multilayer calculation, including large broadening and shift of higher orders due to depth penetration. (c) Linear plot of (b) including  $\sigma$  polarization on the same scale, for first, second and fourth orders. Expected real profiles for PET 00(2n) finite curved perfect-crystal diffraction at  $7.2 \text{ \AA}/n$ , orders  $n = 1, 2, 4$ , neglecting the finite source. (d) Finite-source multilayer results give smooth final profiles on the film (including emulsion shifts). Fourth-order diffraction is scaled by  $(40 \times, 40 \times)$  for (c) ( $\pi, \sigma$ ) and  $(10 \times, 40 \times)$  for (d). Widths are 76, 27, 133 and 126 (2)  $\mu\text{m}$  for first-order  $\pi$  and  $\sigma$  and fourth-order  $\pi$  and  $\sigma$  radiation in (c), respectively, broadened to 76, 36, 140 and 142 (2)  $\mu\text{m}$  in (d).

particular polarizations and lines but would reveal themselves through these parameters or from full profile shapes.

For the above example, values of  $g$  for first-order  $\sigma$  and  $\pi$  radiations and fourth-order  $\sigma$  and  $\pi$  radiations are  $-0.296$ ,  $-0.103$ ,  $-0.0903$ ,  $-0.0317$ , respectively, while  $\kappa = 0.0813$  for first-order and  $0.0136$  for fourth-order radiation. Hirsch & Ramachandran (1950) and Cole & Stemple (1962) give simpler diffraction formulae relating directly to these parameters, with corresponding plots. The differences between the 75th and 25th percentiles for final calculations indicate the scale of diffraction, finite source and geometric defocusing, and show typical variation with diffraction order.

The shift of the peak (channel) relative to the Bragg reference position may be compared with mean shifts. This highlights profile asymmetries in opposite directions for first- and fourth-order diffraction due to flat-crystal asymmetry and depth penetration, respectively, and indicates relatively small differences of means for different polarizations. Values of  $C_\theta$  are derived from mean shifts on each scale. The three values differ: only those using the  $Y_{iz}$  scale include all depth and defocusing effects. A relative error of final  $C_\theta^{Y_{iz}}$  corrections indicates convergence of iterative calculations of  $C_\theta$  from  $C_{Y_{iz}}$ . The curvature  $c$  may be compared with that given by CMRB.

The mean penetration depth  $\bar{d}$  compares with flat-crystal and other estimates, and ensures that sufficient

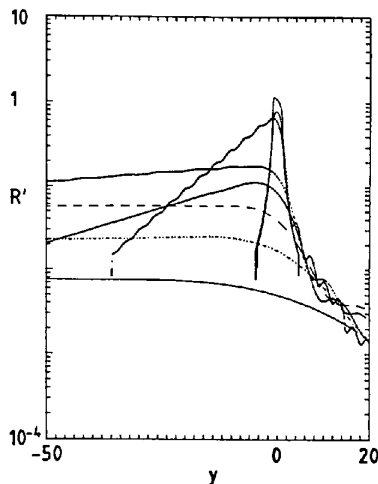


Fig. 14. Finite curved perfect crystal reflectivities  $R'$  versus the diffraction coordinate at the surface  $y(0)$  giving dominant contributions to the  $\theta_2$  angle profile. PET 00(2n),  $7.2 \text{ \AA}/n$ , orders  $n = 1$  to 4,  $\sigma$  and  $\pi$  polarization,  $2Rz = 300 \text{ mm}$ . Point-source multilayer test showing first-order radiation unchanged from finite flat profiles, but reflectivities from higher orders increased dramatically by asymmetric reflection from deep layers; oscillations derive from Pendellösung effects and are not dominated by precision. This shows the continuity and smoothness of  $y(0)$  with  $\theta_2$  and the precision.

regions are used within each crystallite. The crystallite thickness  $t_0$  used in flat- and curved-crystal calculations is also given.  $t_0$  corresponds to  $\Delta y_0$  in the curved crystal across the crystallite thickness, set to the finite flat-crystal diffraction width on the diffraction coordinate scale.

Table 1 shows the grazing-incidence finite flat crystal integrated reflectivity ( $R_C$ ), the curved-crystal integrated reflectivities assuming a point source [ $R_H^{y,x=0}$ , integrating over  $y(0)$  and  $R_H^{\theta_2,x=0}$ ] and the ratio of incident to diffracted powers over the range considered with the finite source [ $R_H^{\theta_2}/(\theta_{\max} - \theta_{\min})$  or  $R_H^{\theta_2} = 2\pi^{I_{\text{out}}/I_0}$  for uniform emission into  $2\pi$  rad]. Mosaic calculations provide equivalent flat-crystal grazing-incidence integrated reflectivity  $R_m$ . Integrated reflectivities for infinite flat crystal calculations are equivalent to  $R_C$ , while  $R_H^{\theta_2}$  is relevant for the experimental geometry. Curved-crystal values  $R_H^{\theta_{\text{inc}}}$  are equivalent to flat-crystal values  $R_C$  and  $R_m$ . This is close to  $R_H^{\theta_2}$  in all cases, but is much larger than flat-crystal  $R_C$  values for higher orders due to depth penetration.

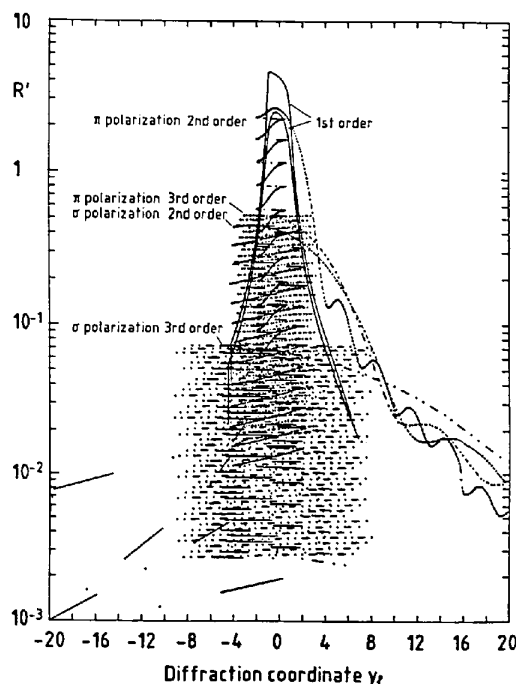


Fig. 15. As Fig. 14 but plotted against diffraction coordinate  $y_1$  for the layer giving the dominant reflectivity component of  $Y_{iz}$  profiles. The point-source single-layer test is similar to Fig. 9(a) but scaled for the focusing geometry. Here the scaling is the same and first-order profiles are unchanged but this multilayer calculation shows clear migration of the dominant reflectivity from the first to second and deeper layers for second-order  $\pi$ -polarized radiation. This is accentuated for higher orders and dominant contributions to some regions of  $Y_{iz}$  profiles arise from 13th and deeper layers. Large central regions of  $R$  versus  $Y_{iz}$   $\theta_2$  profiles are due to  $|y| < \Delta y_0/2$ , with each local peak corresponding to a different source element – so the profile steps from  $-\Delta y_0/2$  to  $+\Delta y_0/2$  and then jumps back, until the tail is reached.

Table 1. Summary of parameters for  $2R = 300$  mm,  $T = 0.4$  mm PET 002 perfect-crystal diffraction

See text and Appendix for variable definitions.

Parameter and scale	Order, polarization			
	1st, $\sigma$	1st, $\pi$	4th, $\sigma$	4th, $\pi$
$\lambda_D$ (Å)	7.1671		1.79469	
$\theta_B$ (rad)	0.96217		0.96450	
$g$	-0.296	-0.103	-0.0903	-0.0317
$\kappa$	0.0813	0.0813	0.0136	0.0136
Difference between the 75th and 25th percentiles				
$\theta_{inc}$ , flat crystal (rad)	$8.66 \times 10^{-5}$	$2.409 \times 10^{-4}$	$2.04 \times 10^{-5}$	$1.88 \times 10^{-5}$
$\theta_s$ (rad)	0.00442	0.00442	0.00442	0.00443
$\theta_2$ (rad)	$8.34 \times 10^{-5}$	$2.417 \times 10^{-4}$	0.000446	0.000465
$Y_{iz}$ ( $\mu\text{m}$ )	37.1	76.2	143.4	144.4
Peak shift with respect to Bragg location				
$\theta_{inc}$ , flat crystal (rad)	$2.21 \times 10^{-4}$	$1.38 \times 10^{-4}$	$1.42 \times 10^{-5}$	$1.42 \times 10^{-5}$
$\theta_s$ (rad)	$1.69 \times 10^{-4}$	$1.56 \times 10^{-4}$	$7.32 \times 10^{-4}$	$7.29 \times 10^{-4}$
$\theta_2$ (rad)	$2.17 \times 10^{-4}$	$1.45 \times 10^{-4}$	$-8.5 \times 10^{-6}$	$-2.2 \times 10^{-6}$
$Y_{iz}$ ( $\mu\text{m}$ )	70.0	54.3	-14.1	-15.7
Mean shift with respect to Bragg location				
$\theta_s$ (rad)	$1.74 \times 10^{-4}$	$1.85 \times 10^{-4}$	$7.69 \times 10^{-4}$	$7.71 \times 10^{-4}$
$\theta_2$ (rad)	$2.11 \times 10^{-4}$	$2.01 \times 10^{-4}$	$-3.34 \times 10^{-4}$	$-3.35 \times 10^{-4}$
$Y_{iz}$ ( $\mu\text{m}$ )	63.7	60.7	-92.2	-92.7
$C_{\theta}^{Y_{iz}}$ correction (rad)	$1.48 \times 10^{-4}$	$1.41 \times 10^{-4}$	$-2.13 \times 10^{-4}$	$-2.14 \times 10^{-4}$
$Y_{iz}$ emulsion shift ( $\mu\text{m}$ )	0.656		3.55	
Curvature $c$	0.0285	0.0286	48.0	48.0
$\bar{d}$ ( $\mu\text{m}$ )	1.47	0.911	149	151
$t_0$ (crystallite) ( $\mu\text{m}$ )	42.8	136	6.83	7.56
Regions per layer, $N_r$	27	60	4	4
$\Delta y_0$	2.47	2.73	29.4	11.4
$R_C$	$6.19 \times 10^{-5}$	$2.51 \times 10^{-4}$	$1.10 \times 10^{-7}$	$9.93 \times 10^{-7}$
$R_H^{y,x=0} = R_H^y$ (0.1 $\mu\text{m}$ )	1.58	2.23	6.57	19.4
$R_H^{\theta,y,x=0} = R_H^{\theta}$	$6.90 \times 10^{-5}$	$2.81 \times 10^{-4}$	$3.83 \times 10^{-6}$	$3.23 \times 10^{-5}$
$R_H^{\theta,pc}$	$6.35 \times 10^{-5}$	$2.59 \times 10^{-4}$	$3.53 \times 10^{-6}$	$2.98 \times 10^{-5}$

These reflectivities allow film exposure to be related to a cylindrically or spherically symmetric photon flux (and excited-state population). Widths, shifts and profiles on the  $Y_{iz}$  scale may be compared with data to give information on polarization and mosaic character of incident radiation and crystals or to yield wavelength estimates.

### 17. Further work

The modelling and theory have passed a series of comprehensive tests. Experimental comparisons for PET and other crystals are given in paper II. Effects of depth penetration, cosine-ratio variation, use of complex formulae, appropriate lamellar thicknesses to account for interference, division of lamellae into multiple regions and inclusion of incoherent scattering have been shown to be significant and important in the derivation of diffraction profiles for curved perfect crystals.

Other comparisons of refractive-index shifts in different orders for curved finite crystals led to prob-

lems from the inadequate nature of our stationary X-ray sources, yielding poor profiles with centroid errors of perhaps 2 parts in  $10^4$ . This is the same magnitude as the corrections and relates to lines whose wavelength centroids are not well defined. Large separations along the film between stationary source and beam spectra prevent accurate estimates of shifts for fast beam lines (since shifts change with Bragg angle and energy) and must be correlated to model estimates of shifts in both regions.

Further tests should include direct comparisons of profiles, shifts and widths to experiment. Previous experiments use double-crystal techniques, convolving the profiles and concentrate on integrated reflectivities for narrow-beam incidence of germanium 111 and quartz 101; these conditions are not directly comparable with our experimental arrangement or with current implementation of theory. Integrated reflectivity is, in any case, a poor test.

The author would like to thank Shell Australia, the Hasselblad Foundation and the Draper's Company

for support of this research, and St Anne's College, Oxford, for a Junior Research Fellowship covering part of the period of research. Acknowledgements go to Drs J. D. Silver, D. D. Dietrich and J. M. Laming for assistance and support, especially on the experimental side of this work.

### APPENDIX Basic notation

$\lambda$ : X-ray wavelength (*in vacuo*).  
 $d$ : crystal-lattice spacing (for index  $H$ ).  
 $2Rz$ : crystal curvature radius along the generatrix ( $Rz$  is the Rowland-circle radius).  
 $\theta_s$ : angle from source with respect to crystal pole (along the generatrix of the cylindrically curved crystal).  
 $\theta_{inc}$ : grazing angle of incidence on crystal surface.  
 $\alpha_1$ : transverse angle of the incident beam with respect to the generatrix.  
 $\theta_1 = \arcsin [(\sin \theta_{inc})/\cos \alpha_1]$ : component of  $\theta_{inc}$  along generatrix.  
 $\theta_{out}$ : grazing angle of emission/reflection at crystal surface.  
 $\theta_2 = \arcsin [(\sin \theta_{out})/\cos \alpha_1]$ : component of  $\theta_{out}$  on generatrix.  
 $\theta_{ik}, k = 1, 2, \dots$ : grazing angle of incidence on  $k$ th lamellar surface.  
 $\theta_{rk}, k = 1, 2, \dots$ : grazing angle of emission from  $k$ th lamellar surface.  
 $\alpha_{plane}$ : (mean) angle of diffracting planes to the lamellar or crystal surface (along the generatrix).  
 $\theta = \theta_{ik} + \alpha_{plane}$ : grazing angle of incidence on crystal planes (see Caciuffo *et al.*, 1987).  
 $\theta_r = \theta_{rk} - \alpha_{plane}$ : grazing angle of reflection on crystal planes.  
 $\theta_B = \arcsin \lambda/2d$ : Bragg angle.  
 $\alpha = 4(\sin \theta_B - \sin \theta) \sin \theta_B \simeq 2(\theta_B - \theta) \sin (2\theta_B)$ .  
 $C$ : polarization factor [ $= 1$  for normal component ( $\pi$  polarization), or  $|\cos 2\theta|$  for  $\sigma$  polarization].  
 $b$ : (approximately) ratio of the discretion cosines ( $\gamma_0, \gamma_H$ ) of incident and diffracted (reflected) beams relative to the normal to the crystal (lamellar) surface.  
 $\psi'_H, \psi''_H$ : real and imaginary parts of the Fourier component of index  $H$  of  $4\pi$  times the polarizability; related to structure factors  $F_H$  by  $\psi_H = -[e^2\lambda^2/(\pi mc^2)]N_0F_H$ ; both parts are summed over real (imaginary) contributions from each scattering centre so may be complex, except for the  $H \equiv 0$  ( $hkl = 000$ ) component parts.  
 $e, m, c, N_0$ : electron charge, electron rest mass, velocity of light, Avogadro's number.  
 $t_0$ : crystal (lamellar) thickness (or penetration depth).  
 $\mu$ : linear absorption coefficient.

$$z = [(1 - b)/2]\psi_0 + (b/2)\alpha.$$

$$q = C^2 b \psi_H \psi_H.$$

$$a = \pi t_0 / (\lambda \gamma_0).$$

$$v + iw = (q + z^2)^{1/2}.$$

$$y = \text{Re}(z) / (|b|^{1/2} |C\psi'_H|)$$

$$= \{[(1 - b)/2]\psi'_0 + (b/2)\alpha\} / (|b|^{1/2} |C\psi'_H|):$$

the deviation parameter.

$$g = \text{Im}(z) / (|b|^{1/2} |C\psi'_H|)$$

$$= [(1 - b)/2]\psi''_0 / (|b|^{1/2} |C\psi'_H|).$$

$y(0)$ : value of  $y$  at crystal surface.

$$\kappa = |\psi''_H| / |\psi'_H|.$$

$$A = \pi |C\psi'_H| t_0 / (\lambda |\gamma_0 \gamma_H|^{1/2}).$$

$P_0^e$ : power incident at the crystal surface.

$I_0^e$ : intensity of the incident beam.

$P_e^0, I_e^0, P_H, I_H$ : power and intensity of the transmitted beam and of the diffracted beam of index  $H$ .

$$R_H^y = \int (P_H/P_0^e) dy = \int r dy:$$

integrated reflectivity on  $y$  scale.

$$R_H^\theta = \int (P_H/P_0^e) d(\theta - \theta_B)$$

$$\simeq [|C\psi'_H| / (|b|^{1/2} \sin 2\theta_B)] R_H^y:$$

integrated reflectivity on grazing-incidence-angle scale.

$$R_C = \int_0^{\pi/2} r d\theta_{inc} = \sum_{\text{step}=1}^n r(\theta_{\max f} - \theta_{\min f})/n:$$

grazing-incidence finite flat crystal reflectivity.

$$R_H^{y,x=0} = \int_{-\infty}^{+\infty} r dy = R_H^{\theta_s, x=0} \overline{\delta y / \delta \theta_s}:$$

curved-crystal integrated reflectivity on the  $y$  scale, assuming a point source and neglecting the Gaussian spread.

$$R_H^{\theta_s, x=0} = \frac{1}{2} \int_0^{2\pi} r d\theta_s = \sum_{\text{step}=1}^n r(\theta_{\max} - \theta_{\min})/n:$$

curved-crystal integrated reflectivity on the  $\theta_s$  scale, assuming a point source and neglecting the Gaussian spread.

$$R_H^{\theta_s} = \frac{1}{2} \int_0^{2\pi} \int_0^x r P(x) dx d\theta_s$$

$$= \sum_{\text{step } \theta_s = 1}^{n1} \sum_{\text{step } x = 1}^{n2} r P_s(x) (\theta_{\max} - \theta_{\min})/n:$$

curved-crystal integrated reflectivity on the  $\theta_s$  scale.

### References

- BATTERMAN, B. W. & COLE, H. (1964). *Rev. Mod. Phys.* **36**, 681-717  
 BEARDEN, J. A., MARZOLF, J. G. & THOMSEN, J. S. (1968). *Acta Cryst.* **A24**, 295-301.  
 BEYER, H. F. & LIESEN, D. (1988). *Nucl. Instrum. Methods*, **A272**, 895-905.

- BOEUF, A., LAGOMARSINO, S., MAZKEDIAN, S., MELONE, S., PULITI, P. & RUSTICHELLI, F. (1978). *J. Appl. Cryst.* **11**, 442–449.
- BUREK, A. J. (1976). *Space Sci. Instrum.* **2**, 53–104.
- BUREK, A. J., BARRUS, D. M. & BLAKE, R. L. (1974). *Astro-phys. J.* **191**, 533–543.
- CACIUFFO, R., MELONE, S., RUSTICHELLI, F. & BOEUF, A. (1987). *Phys. Rep.* **152**, 1–71.
- CHANTLER, C. T. (1990). DPhil thesis, Univ. of Oxford, England.
- CHUKHOVSKII, F. N., GABRIELIAN, K. T., KISLOVSKII, E. N. & PROKOPENKO, I. V. (1987). *Phys. Status Solidi A*, **103**, 381–387.
- CHUKHOVSKII, F. N., GABRIELIAN, K. T. & PETRASHEN', P. V. (1978). *Acta Cryst.* **A34**, 610–621.
- CHUKHOVSKII, F. N. & MALGRANGE, C. (1989). *Acta Cryst.* **A45**, 732–738.
- CHUKHOVSKII, F. N. & PETRASHEN', P. V. (1977). *Acta Cryst.* **A33**, 311–319.
- COLE, H. & STEMPLE, N. R. (1962). *J. Appl. Phys.* **33**, 2227–2233.
- DESLATTES, R. D., TORGESON, J. L., PARETZKIN, B. & HORTON, A. T. (1966). *J. Appl. Phys.* **37**, 541–548.
- EILERMAN, D. & RUDMAN, R. (1979). *Acta Cryst.* **B35**, 2458–2460.
- EROLA, E., ETELÄNIEMI, V., SUORTTI, P., PATTISON, P. & THOMLINSON, W. (1990). *J. Appl. Cryst.* **23**, 35–42.
- EWALD, P. P. (1916). *Ann. Phys. (Leipzig)*, **49**, 1–38, 117–143.
- FROLOV, A. P., VERESHCHAGIN, L. F. & RODIONOV, K. P. (1962). *Sov. Phys. Solid State*, **4**, 1178–1182.
- HALL, R. (1980). PhD thesis, Univ. of Leicester, England.
- HENKE, B. L., LEE, P., TANAKA, T. J., SHIMABUKURO, R. L. & FUJIKAWA, B. K. (1982). *At. Data Nucl. Data Tables*, **27**, 1–144.
- HIRSCH, P. B. & RAMACHANDRAN, G. N. (1950). *Acta Cryst.* **3**, 187–194.
- International Tables for X-ray Crystallography* (1974). Vol. IV, §2.2, pp.71–102. Birmingham: Kynoch Press. (Present distributor Kluwer Academic Publishers, Dordrecht.)
- International Tables for X-ray Crystallography* (1983). Vol. III. Birmingham: Kynoch Press. (Present distributor Kluwer Academic Publishers, Dordrecht.)
- JAMES, R. W. (1963). *Solid State Phys.* **15**, 53–220.
- KÄLLNE, E. & ABERG, T. (1975). *X-ray Spectrosc.* **4**, 26–27.
- KALMAN, Z. H. & WEISSMAN, S. (1983). *J. Appl. Cryst.* **16**, 295–303.
- KATAGAWA, T. & KATO, N. (1974). *Acta Cryst.* **A30**, 830–836.
- KATO, N. (1960). *Acta Cryst.* **13**, 349–356.
- LAMING, J. M. (1988). DPhil thesis, Univ. of Oxford, England.
- LAUE, M. VON (1949). *Acta Cryst.* **2**, 106–113.
- POPOVICI, M., STOICA, A. D., CHALUPA, B. & MIKULA, M. (1988). *J. Appl. Cryst.* **21**, 258–265.
- SUORTTI, P. & FREUND, A. K. (1989). *Rev. Sci. Instrum.* **60**, 2579–2585.
- SUORTTI, P., PATTISON, P. & WEYRICH, W. (1986). *J. Appl. Cryst.* **19**, 336–342.
- TAKAGI, S. (1969). *J. Phys. Soc. Jpn*, **26**, 1239–1253.
- TAUPIN, D. (1964). *Bull. Soc. Fr. Minéral. Cristallogr.* **87**, 469–511.
- VIEGELE, W. J. (1973). *At. Data*, **5**, 51–111.
- VIEGELE, W. J. (1974). In *CRC Handbook of Spectroscopy*, Vol. I, edited by J. W. ROBINSON, pp. 28–213. Boca Raton, Florida: CRC Press.
- WHITE, J. E. (1950). *J. Appl. Phys.* **21**, 855–859.
- WILKINS, S. W. (1978). *Acta Cryst.* **A34**, 343–344.
- ZACHARIASEN, W. H. (1945). *Theory of X-ray Diffraction in Crystals*. New York: Wiley.